NEPTUNE AND TRITON

Dale P. Cruikshank
Editor

With the editorial assistance of
M. S. Matthews and A. M. Schumann

With 78 collaborating authors

THE UNIVERSITY OF ARIZONA PRESS
TUCSON

About the cover:

The front cover shows Neptune as seen from the surface of Triton. Contorted icy materials in a region of vents form the foreground. Beyond the horizon in this telephoto view is an active vent and plume, whose smoky trail crosses the 8° disk of Neptune. The sub-Triton latitude on Neptune is near its maximum value of about 23°, as seen from this point in Triton's inclined orbit. Painting by Ron Miller and William K. Hartmann.

About the back cover:

The back cover shows a schematic of Neptune's magnetosphere. The exterior bow shock and magnetopause boundaries are highlighted. Within the interior regions are shown the radiation belt, the orbit of the satellite Triton, the position of the outer ring, 1989N1R, and the orientation of the internal magnetic configuration (**M**) with respect to the spin axis of Neptune (Ω). Magnetic field lines are shown with black lines with embedded arrows. The trajectory of the Voyager 2 Spacecraft is shown also on the figure. Because of the planet's rapid spin, the configuration of the magnetosphere changes rapidly. The configuration shown is valid for the time that Voyager 2 crossed the inbound magnetopause, and 16.1 hours later. See the Chapter by Mauk et al.

The University of Arizona Press

♾ This book is printed on acid-free, archival-quality paper.
Manufactured in the United States of America.

99 98 97 96 95 7 6 5 4 3 2 1

Library of Congress Cataloging-in-Publication Data

Neptune and Triton / D.P. Cruikshank, editor.
p. cm. — (Space science series)
"Principal result of a conference held in Tucson, Arizona, January 6–10, 1992."—Introd.
Includes bibliographical references and index.
ISBN 0-8165-1525-5 (cloth : acid free paper)
1. Neptune (Planet) 2. Triton (Satellite) 3. Voyager Project.
I. Cruikshank, Dale P. II. Series.
QB691.N46 1996
523.4'5—dc20 95-32468
CIP

British Library Cataloguing-in-Publication Data
A catalogue record for this book is available from the British Library.

PLASMA WAVES AND RELATED PHENOMENA IN THE MAGNETOSPHERE OF NEPTUNE

D. A. GURNETT and W. S. KURTH
University of Iowa

On 25 August 1989, Voyager 2 flew by Neptune, thereby providing the first measurements of particles and fields in the vicinity of Neptune. In this chapter we describe the results from the plasma-wave investigation. The plasma-wave instrument detected many familiar phenomena. These include electron plasma oscillations upstream of the bow shock, broadband electric field noise at the bow shock, electron cyclotron harmonic waves and upper hybrid emissions at the magnetic equator crossings, dust impacts, whistlers, and various complex plasma-wave phenomena in the inner magnetosphere. Generally, the field strengths were quite weak, typically in the range from 10 to 100 $\mu V\ m^{-1}$. The strongest noise observed during the entire flyby was caused by dust impacts on the spacecraft, which reached peak intensities near the two equator crossings. The dust particles are believed to have radii on the order of 10 μm and peak number densities at the inbound and outbound ring plane crossings of 1.0×10^{-2} and $4 \times 10^{-3}\ m^{-3}$, respectively. The interpretation of the plasma waves in the inner magnetosphere is complicated by the lack of definitive information on the electron density profile in the region near closest approach. Various plasma-wave cutoffs and resonances have been used to place limits on the electron density in this region. These limits indicate that the spacecraft passed through a region of dense cold ionospheric plasma near closest approach with electron densities of at least 30 cm^{-3}, and possibly as high as 500 cm^{-3}.

I. INTRODUCTION

The Voyager 2 flyby of Neptune on 25 August 1989, provided the first opportunity to obtain particle and fields measurements in the vicinity of Neptune. In this chapter we review the results from the plasma-wave instrument, which provided electric field measurements over a frequency range from 10 Hz to 56 kHz. Although this review is primarily concerned with plasma waves, it also includes a discussion of radio emissions, dust impacts, and various other related phenomena.

Before proceeding with a description of the observations, it is useful to review briefly the relevant instrumentation and the details of the spacecraft trajectory. The plasma-wave instrument, sometimes abbreviated PWS (plasma-wave subsystem), shares an electric antenna with the planetary radio astronomy instrument, usually abbreviated PRA. The common antenna consists of two orthogonal 10-m elements mounted on the spacecraft as shown in

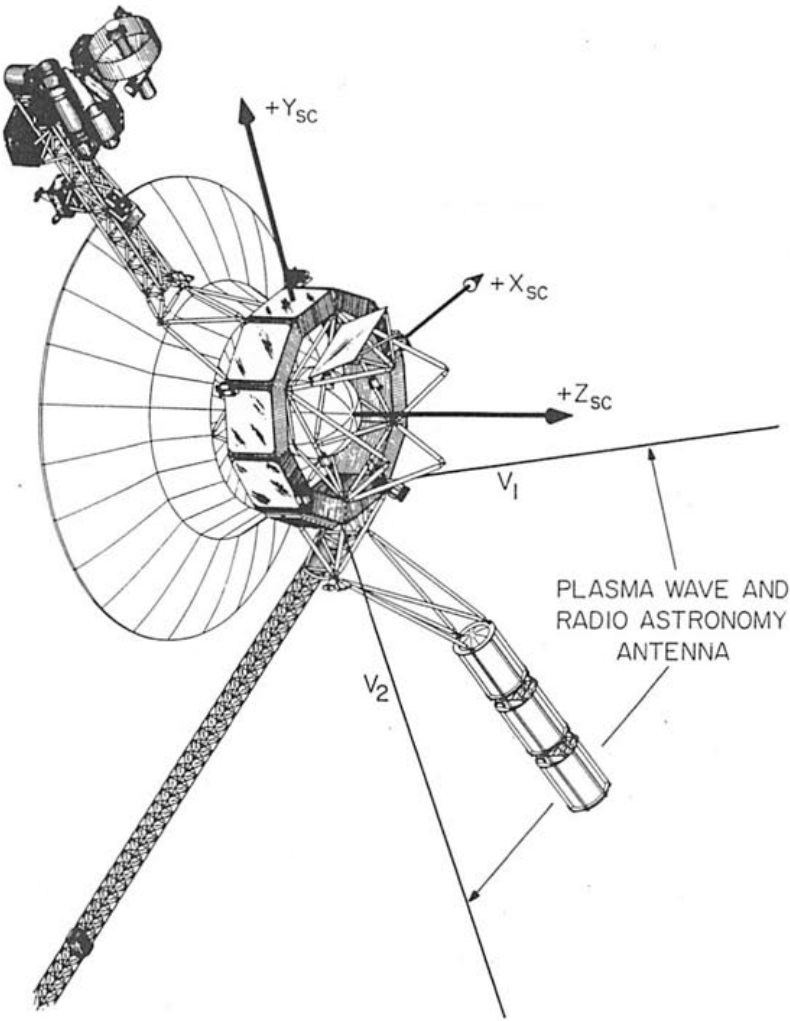

Figure 1. A sketch of the Voyager spacecraft showing the location of the two 10-m electric antenna elements. The plasma-wave instrument uses these elements as a balanced dipole, and the planetary radio astronomy instrument uses them as two independent monopoles.

Fig. 1. The plasma-wave instrument is intended to provide measurements in the low-frequency (plasma wave) part of the spectrum, from 10 Hz to 56 kHz, and the radio astronomy instrument is primarily intended to provide measurements in the high-frequency (radio) part of the spectrum, from ~20 kHz to 40 MHz. For a description of the plasma-wave instrument see Scarf and Gurnett (1977), and for a description of the radio astronomy instrument see Warwick et al. (1977). The plasma-wave instrument uses the two antenna el-

ements as a balanced dipole (i.e., it responds to the voltage difference, $\Delta V = V_1 - V_2$, between the two elements), whereas the radio astronomy instrument uses the antennas as two independent monopoles. The electric field strength, E, is calculated using $E = \Delta V/\ell_{\text{eff}}$, where ℓ_{eff} is the effective length. At low frequencies the effective length is assumed to be the distance between the center of the two elements, which is ~7 m.

The plasma-wave instrument processes signals from the electric antenna in two ways. First, a 16-channel spectrum analyzer is used to provide essentially continuous low-resolution field strength measurements from 10 Hz to 56 kHz. The 16-channel analyzer provides one complete scan of the spectrum every 4 s and has four logarithmically spaced channels per decade. Second, a wideband receiver, with a bandwidth of 50 Hz to 10 kHz, is used to provide high-resolution waveform measurements over selected time intervals. The wideband system provides 4-bit samples of the electric field waveform at a rate of 28,800 samples per second. An automatic gain control with a time constant of 0.5 s is used to maintain the output waveform within the dynamic range of the 4-bit analog-to-digital converter. Because of the automatic gain control, absolute field strengths cannot be obtained from the wideband receiver. Absolute intensities can only be obtained from the 16-channel spectrum analyzer. Because the data rate of the wideband measurements (115.2 kb s^{-1}) greatly exceeds the spacecraft telemetry rate at Neptune, these data must be stored on the spacecraft tape recorder and transmitted later at a lower data rate. For this reason wideband data can only be collected for short intervals, usually not longer than 48 s (one telemetry frame). A total of 82 wideband recordings were obtained in Neptune's magnetosphere. These consisted of twenty-five 48-s recordings, ten 10-s recordings, and forty-seven 5-s recordings. On the ground the waveforms can be either displayed directly, or Fourier transformed to provide high-resolution frequency-time spectrograms.

To help interpret the observations, a sketch of the spacecraft trajectory past Neptune is shown in Fig. 2. The spacecraft approached Neptune from the sunward side of the planet at a local time of ~13.0 hr, crossed the equatorial plane from south to north on the inbound pass at a radial distance of 3.45 R_N (1 R_N = 24,762 km) at 0253:01.6 spacecraft event time (SCET), and then passed over the northern polar region, reaching a maximum latitude of 77.6°. Shortly after passing over the northern polar region, the spacecraft reached a closest approach radial distance of 1.18 R_N at 0355:59.3 SCET. On the outbound pass the spacecraft again crossed the equatorial plane, this time from north to south, at a radial distance of 4.20 R_N at 0514:52.8 SCET, finally receding away from the planet at a local time of ~0.2 hr.

Also of interest is the trajectory relative to the magnetic field. Because Neptune's magnetic dipole has a large tilt (47°) and offset (0.55 R_N) from the center of the planet (Ness et al. 1989), the trajectory through the magnetic field is quite complicated. For a detailed discussion of Neptune's magnetic field, see Connerney et al. (1991; see also Chapter by Ness et al.). The main results of interest for this review are that the magnetic field is quite strong and

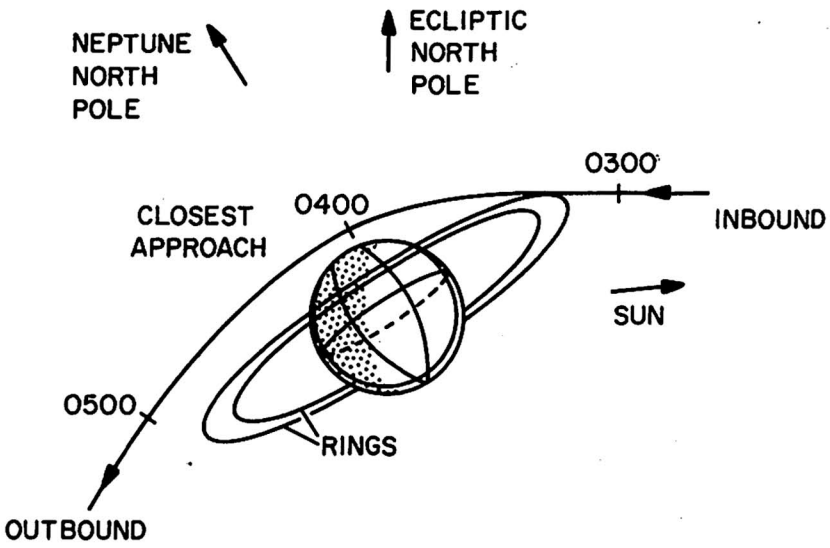

Figure 2. A sketch of the spacecraft trajectory by Neptune. The spacecraft crossed through the equatorial plane twice, the first time on the inbound pass at ~3.45 R_N, and the second time on the outbound pass at ~4.20 R_N.

can be approximated by a dipole over a substantial range of radial distances (roughly 4 to 15 R_N; see Ness et al. 1989). The maximum magnetic field strength occurred at 0355:39 SCET, just before closest approach, and was 9950 nT, which corresponds to an electron cyclotron frequency of 279 kHz ($f_c = 28\,|B|$ Hz, where B is in nT). The offset-tilted-dipole (OTD2) model of Ness (personal communication), shows that three magnetic equator crossings occurred near the planet, the first on the inbound leg at a radial distance of 10.2 R_N at 0023 SCET, the second near closest approach at a radial distance of 1.8 R_N at 0421 SCET (quite uncertain because of the non-dipolar nature of the field near closest approach), and the third on the outbound leg at a radial distance of 11.4 R_N at 0757 SCET.

In order to organize the discussion, the results are described more or less in the order in which the observations were obtained, starting with upstream waves detected during the approach to the planet, and ending with various phenomena observed in the inner regions of the magnetosphere. Because no plasma wave phenomena are known to have been associated with Neptune's moon, Triton, the data obtained in the vicinity of this moon are not discussed.

II. UPSTREAM WAVES, BOW SHOCK, AND MAGNETOPAUSE

The first evidence of plasma waves associated with the magnetosphere of Neptune occurred at 1055 spacecraft event time (SCET) on 25 August 1989. At this time weak bursts of electron plasma oscillations started to occur in the

562 Hz channel of the 16-channel spectrum analyzer. From previous studies at other planets (Scarf et al. 1971,1979*a*,1979*b*; Gurnett et al. 1981*a*,1986; Grard et al. 1991), it is known that electron plasma oscillations are produced at a characteristic frequency known as the electron plasma frequency ($f_{pe} = 8980\sqrt{n_e}$ Hz, where n_e is the electron density in cm^{-3}) by electrons streaming outward into the solar wind from the bow shock. Comparisons with the Voyager plasma measurements (Richardson et al. 1991) confirm that the emission frequency is at the local electron plasma frequency. It is well known that plasma oscillations occur in a region upstream of the shock known as the foreshock, which is the region of the solar wind accessible to electrons emitted from the shock. A sketch of the foreshock is shown in Fig. 3. Because electrons are guided along the solar wind magnetic field, the sunward boundary of the foreshock is a magnetic field line (in three dimensions, a surface) tangent to the bow shock (Filbert and Kellogg 1979). The onset of electron plasma oscillations at 1055 SCET therefore indicated that the spacecraft had passed into the electron foreshock. In this case, the crossing into the foreshock was probably controlled more by changes in the solar wind magnetic field orientation than by the motion of the spacecraft. In fact, after a few sporadic bursts, the plasma oscillations ceased, indicating that the spacecraft was no longer magnetically connected to the bow shock. The occurrence of plasma oscillations, together with measurements of the solar wind magnetic field direction can be used as a tool for remotely sensing the geometry and location of Neptune's bow shock. For a discussion of this technique, see Cairns et al. (1991).

About an hour and a half after the initial sporadic encounter with the foreshock, the plasma oscillations again reappeared in the 562 Hz channel at 1252 SCET, this time nearly continuous and much stronger ($\sim 100\,\mu\mathrm{Vm}^{-1}$). The onset of these plasma oscillations can be seen in Fig. 4, which shows the electric field intensities in the bottom 9 channels of the 16-channel spectrum analyzer. The higher intensities and nearly constant amplitude indicated that the spacecraft was much closer to the shock. Indeed, about an hour and three-quarters later, at 1435 SCET, the spacecraft crossed the bow shock. The bow shock can be easily identified in Fig. 4 by the abrupt burst of broadband electric field noise, which is characteristic of all planetary bow shock crossings (Fredricks et al. 1968; Scarf et al. 1979*a*,1979*b*; Gurnett et al. 1981*a*,1986; Grard et al. 1991). This shock identification also agrees well with the shock crossing time of 1438 SCET given by the magnetic field and plasma investigations (Ness et al. 1989; Belcher et al. 1989).

The broadband electric field strength at the shock is $\sim 30\,\mu\mathrm{Vm}^{-1}$, which in absolute terms is the weakest of any of the subsolar planetary bow shocks encountered by Voyager. However, in a comparison with other bow shocks, Moses et al. (1990) showed that if the electric field energy density, $E^2/8\pi$, is normalized by dividing by the plasma energy density, $\mathrm{nm}v_{sw}^2$, then the normalized electric field intensities are among the strongest observed at any planet. As can be seen from Fig. 4, the electric field turbulence at the shock

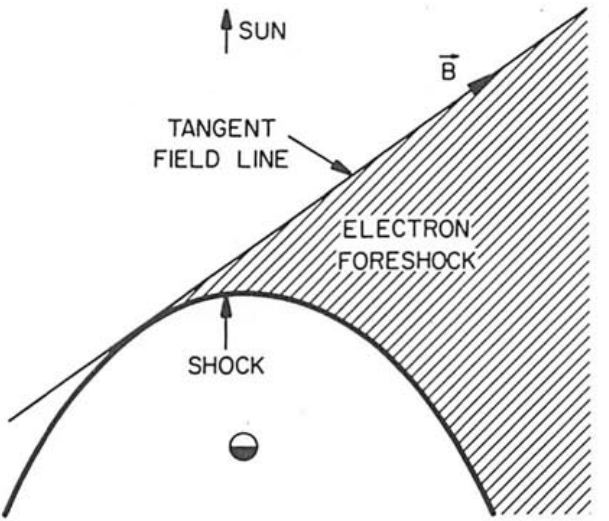

Figure 3. A sketch showing the relationship between the electron foreshock and the bow shock. The sunward boundary of the electron foreshock is determined by the magnetic field lines tangent to the shock. Energetic electrons from the shock escape upstream into the foreshock, thereby producing electron plasma oscillations.

lasted ~10 min, which is the longest of any of the subsolar shock crossings observed by Voyager. The relatively long duration suggests that the shock transition region is thicker than at other planets of the solar system. All of the characteristic length scales that control the thickness of a shock (mainly the cyclotron radius of the reflected ions, $m_i v_{sw}/eB$) increase with increasing radial distance from the Sun, so a thicker shock transition is to be expected at Neptune. However, the interpretation of the shock thickness is complicated by radial motions of the shock, which could distort the apparent thickness.

As the spacecraft passed from the shock into the magnetosheath, the electric field intensities again dropped to very low levels and remained low throughout the magnetosheath. The absence of detectable plasma waves in the magnetosheath is typical of all of the outer planets, but is in marked contrast to the magnetosheaths of Venus, Earth and Mars which have considerable wave activity. The reason for the marked difference in the magnetosheath noise levels between the inner and outer planets is not known. Approximately 5 hr after the shock crossing, both the magnetic field and plasma instruments (Ness et al. 1989; Belcher et al. 1989) showed that the spacecraft entered the magnetosphere through a broad disordered transition region lasting from ~1800 to 1935 SCET. No evidence of the magnetopause crossing can be seen in the plasma-wave data. The absence of a detectable plasma-wave effect at the magnetopause is somewhat unusual, as such crossings at other planets are usually associated with a burst of broadband electric field turbulence and the onset of trapped continuum radiation. However, this entry into the

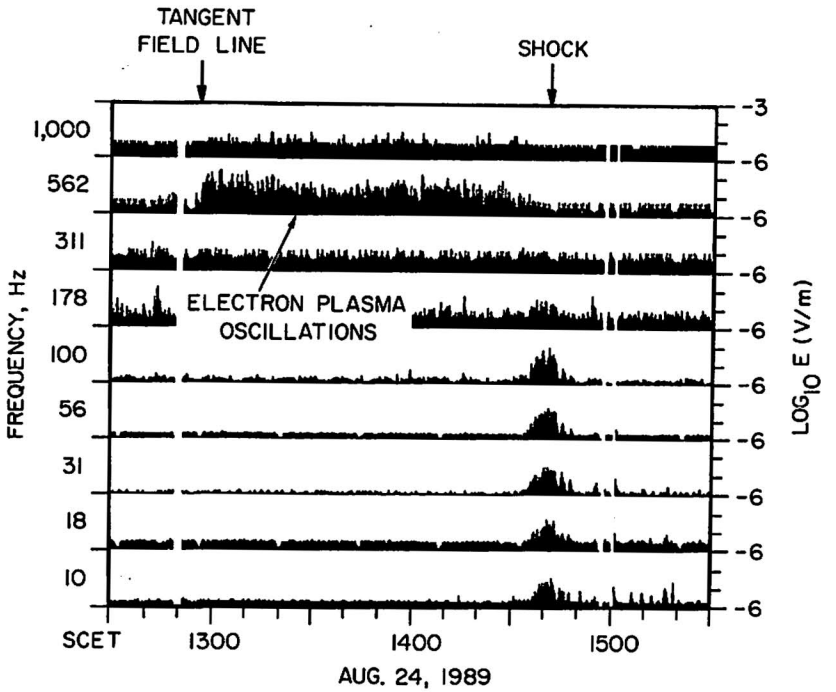

Figure 4. The electric field intensities in the 10 Hz through 1.0 kHz channels of the plasma-wave spectrum analyzer. The narrowband signals in the 562 Hz channel are electron plasma oscillations excited by electrons streaming into the solar wind from the bow shock. The broadband burst of electric field noise from ~1435 to 1443 SCET is caused by the bow shock (figure from Gurnett et al. 1989).

magnetosphere was somewhat unusual. Belcher et al. (1989) have pointed out that because of the large tilt of the planetary dipole axis and rather fortuitous timing, the spacecraft apparently entered the magnetosphere via the polar cusp. This geometry, which was unique for the Voyager flybys of the outer planets, led to a very gradual transition from the dense magnetosheath plasma to the much lower densities characteristic of the magnetosphere. This gradual transition may explain the absence of broadband electric field turbulence at the magnetopause, because this turbulence is often associated with steep density gradients. If any continuum radiation exists trapped within the magnetospheric cavity, it was too weak to be detected.

III. ELECTRON CYCLOTRON AND UPPER HYBRID WAVES

To provide an overview of the plasma waves within the magnetosphere of Neptune, a plot of the electric field intensities from the 16-channel spectrum is shown in Fig. 5. This plot covers a 32-hr period centered on closest approach, starting at ~42 R_N inbound and ending at ~42 R_N outbound. The

upstream electron plasma oscillations and the broadband noise at the shock can be seen in the lower left-hand corner of the plot. The locations of the shock, the magnetopause, the two ring plane crossings, and the Triton closest approach are shown along the top of the plot. Immediately after the magnetopause crossing the only signals that can be detected are some very weak radio emissions in the 5.62 kHz to 56.2 kHz channels. The intensity of these radio emissions increases slowly as the spacecraft approaches the planet. For a discussion of these and other radio emissions observed during the Neptune flyby, see the Chapter by Zarka et al.

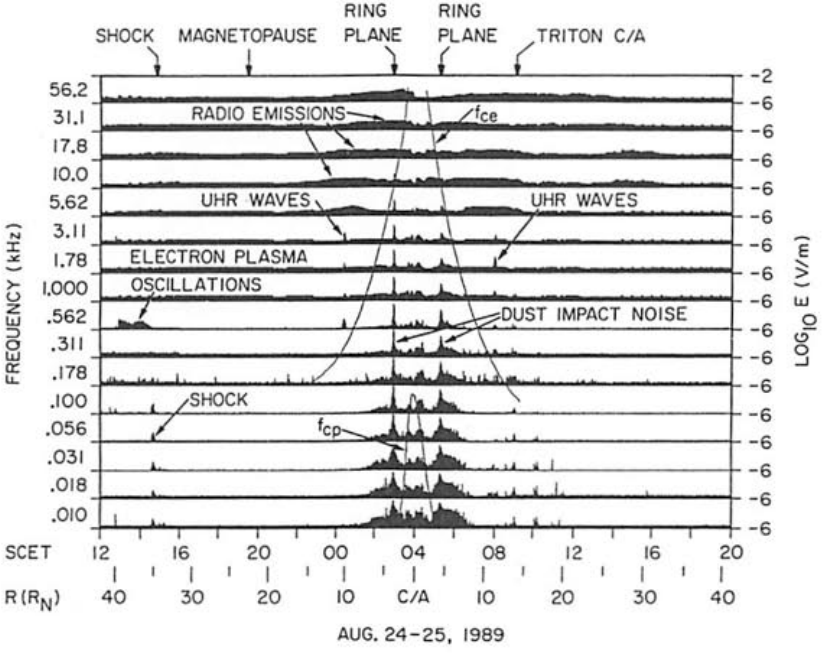

Figure 5. An overview of the 16-channel plasma wave electric field intensities starting at about 42 R_N on the inbound pass and ending at about 42 R_N on the outbound pass. The most intense noise detected by the plasma-wave instrument was caused by dust impacts at the two ring plane crossings (figure from Gurnett et al. 1989).

The first plasma wave emission observed within the magnetosphere occurred at 0023 SCET at a radial distance of 10.2 R_N. At this time, a brief but intense burst of electric field noise was observed in the 562 Hz, 1.00 kHz, 1.78 kHz and 3.11 kHz channels of the 16-channel spectrum analyzer. This noise is most intense in the 562 Hz and 3.11 kHz channels, and lasted ~10 min. The time of peak intensity (0023 SCET) coincided almost exactly with the magnetic equator crossing as determined from the OTD2 magnetic field model. A 1-hr plot illustrating the structure of this noise in the vicinity of

the magnetic equator is shown in Fig. 6. The magnetic latitude, λ_m, computed from the OTD2 magnetic field model is shown along the bottom of the plot. The intense burst of noise at the magnetic equator is seen to consist of enhancements at 562 Hz and 3.11 kHz, and somewhat weaker emissions at 1.00 kHz and 1.7 kHz. The enhanced emission at 562 Hz is slightly above the electron cyclotron frequency, which is indicated by the solid dark line marked f_{ce}. The enhancement at 3.11 kHz is very close to the electron plasma frequency, as determined by density measurements from the plasma instrument (Belcher et al. 1989).

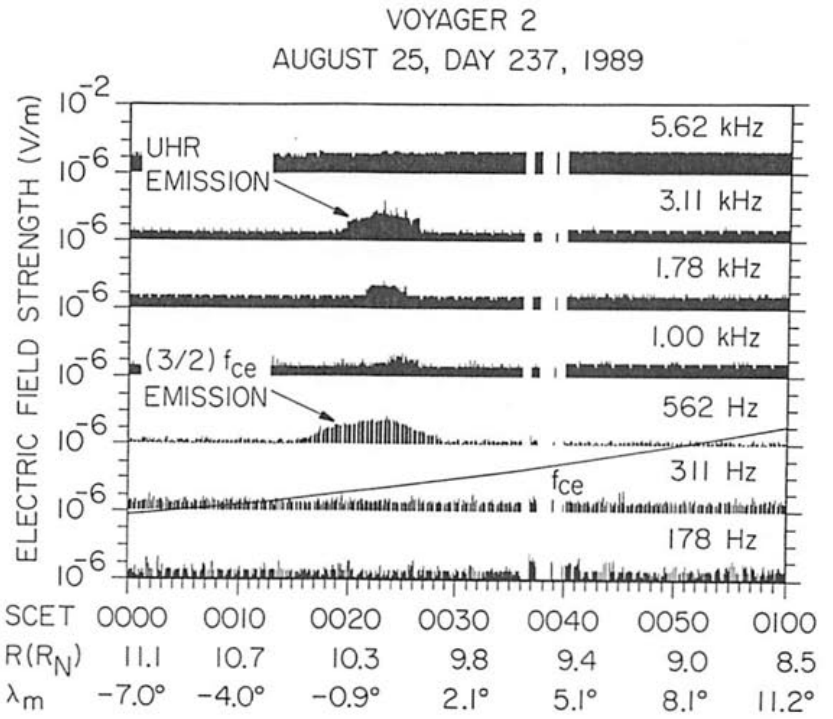

Figure 6. An expanded time scale plot showing the details of the $(3/2)f_{ce}$ electron cyclotron waves and upper hybrid resonance (UHR) emissions observed near the inbound magnetic equator crossing at 10.2 R_N (figure adapted from Barbosa et al. 1990).

Equatorially confined plasma-wave emissions of the type shown in Fig. 6 are a common feature of planetary magnetospheres. At Earth these emissions are known to consist of electrostatic waves near half-integral harmonics of the electron cyclotron frequency, $(n + 1/2)f_{ce}$, where n is an integer (Kennel et al. 1970). The emissions are usually most intense at the low-order harmonics, i.e., near $(3/2)f_{ce}$ and $(5/2)f_{ce}$, and then intensify again near the upper hybrid resonance frequency, $f_{UHR} = \sqrt{f_{ce}^2 + f_{pe}^2}$ (Shaw and Gurnett 1975; Hubbard

and Birmingham 1978; Christiansen et al. 1978; Abdalla and Kennel 1978*a*, *b*; Rönnmark et al. 1978). The waves near the half-integral harmonics are usually called electron cyclotron harmonic (ECH) waves, and the intensification near the upper hybrid frequency is usually called the upper hybrid resonance (UHR) emission. Electron cyclotron harmonic waves and upper hybrid resonance emissions have been observed at Jupiter (Scarf et al. 1979*b*; Kurth et al. 1980), Saturn (Gurnett et al. 1981*a*; Kurth et al. 1983), and Uranus (Gurnett et al. 1986; Kurth et al. 1987). In all cases the waves are very closely confined to the magnetic equator. It is this equatorial confinement, as well as the overall features, that allows us to identify confidently the emissions in Fig. 6 as electron cyclotron harmonic waves and upper hybrid emissions. Unfortunately, no wideband data is available to confirm the detailed harmonic structure. The strong emission in the 562 Hz channel, just above the electron cyclotron frequency, f_{ce}, is most likely the lowest-order electron cyclotron wave at $(3/2)f_{ce}$, and the strong emission in the 3.11 kHz channel is almost certainly the upper-hybrid-resonance emission. The identification of the upper hybrid resonance emission is supported by the plasma instrument which gives an electron density of 0.12 cm^{-3} at this time, which corresponds to an upper hybrid frequency of ~3.2 kHz. The weak responses in the 1.0 kHz and 1.78 kHz channels are probably due to intermediate order harmonics that are only weakly excited.

On the outbound pass, a very similar brief burst of noise can be seen in Fig. 5 at ~0800 SCET at a radial distance of ~11.5 R_N. This noise is also located very close to a magnetic equator crossing (which according to the OTD2 model occurred at 0757 SCET), and is believed to consist of electron cyclotron harmonic waves and upper-hybrid-resonance emissions. Two peaks occur in the spectrum, one at 311 Hz and the other at 1.78 kHz. The peak at 311 Hz is believed to correspond to the lowest-order electron cyclotron harmonic at $(3/2)f_{ce}$, and the peak at 1.78 kHz is believed to correspond to the upper-hybrid emission. Weak responses are also present in the intermediate channels, presumably due to other intermediate-order harmonics.

Although the electron-cyclotron-harmonic waves and upper-hybrid emissions were only observed twice, once on the inbound pass and once on the outbound pass, they are almost certainly present over the entire region near the magnetic equator. These waves are believed to play two important roles in the physics of planetary magnetospheres. First, as pointed out by Kennel et al. (1970), electron cyclotron waves cause pitch-angle scattering of resonant electrons thereby contributing to the precipitation and loss of these electrons. Typically the resonant energies are quite low, on the order of 10 to 100 eV. Second, as pointed out by various authors (see, e.g., Gurnett 1975; Gurnett and Frank 1976; Jones 1976,1980) upper-hybrid-resonance emissions provide a source of escaping electromagnetic radiation via mode conversion. This process for generating radio emissions is a common feature of planetary magnetospheres. At Neptune, the weak radio emissions evident in the 5.62 kHz to 56.2 kHz channels of Fig. 5 are most likely produced by this

mode conversion process (Gurnett et al. 1989). Based on studies of terrestrial continuum radiation by Morgan and Gurnett (1991), the radiation is expected to escape outward into a pancake-like beam oriented along the magnetic equatorial plane, as illustrated in Fig. 7. Studies by Kurth et al. (1990) of the low-frequency Neptunian radio emissions show that the radiation has a beaming pattern very similar to that indicated in Fig. 7, with a beamwidth of $\sim\pm 12°$ relative to the magnetic equator. Because the upper-hybrid-resonance frequency varies continuously with radial distance, a nearly continuous radio emission spectrum should be produced. With the resolution available from the plasma-wave instrument, which has four channels per decade, the spectrum of the low-frequency radio emission appears to be essentially continuous. For this reason the radiation has been referred to as continuum radiation (Gurnett et al. 1989; Kurth et al. 1990; Gurnett et al. 1992). For further discussion of the low-frequency continuum, see the chapter on radio emissions by Zarka et al.

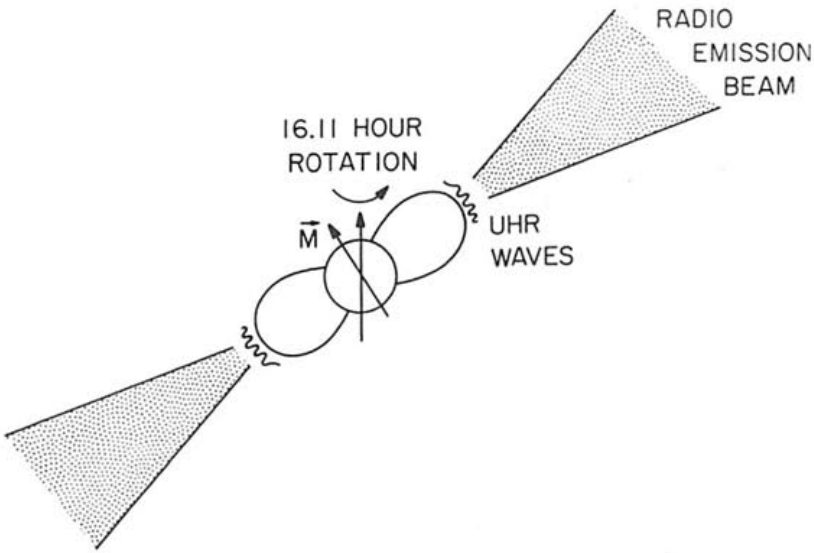

Figure 7. An illustration showing the generation of low-frequency (5 to 50 kHz) radio emissions via mode conversion from electrostatic upper-hybrid-resonance (UHR) waves. The equatorial location of the UHR waves causes the radiation to be directed into a disk-like beam along the magnetic equatorial plane (figure from Gurnett et al. 1992).

IV. DUST IMPACT NOISE

The most intense signals detected by the plasma-wave instrument during the Neptune flyby were caused by dust impacts (Gurnett et al. 1989). Dust impacts are responsible for the two intense peaks at the points marked "ring

plane" in Fig. 5, and for most of the impulsive low-frequency noise inside of $\sim 8\,R_N$. This noise was also detected at higher frequencies by the planetary radio astronomy instrument (Warwick et al. 1989).

Dust impact noise is an ionization effect that occurs when a small, micron-sized particle hits the spacecraft at a high velocity. This noise was first discovered at the Voyager 2 Saturn ring plane crossing when the plasma wave and radio astronomy instruments (Scarf et al. 1982; Warwick et al. 1982; Gurnett et al. 1983*a*; Aubier et al. 1983) detected impulsive signals caused by particles striking the spacecraft. Similar effects were also observed during the Voyager 2 ring plane crossing at Uranus (Gurnett et al. 1986,1987; Warwick et al. 1986; Meyer-Vernet et al. 1986). When a small dust grain strikes the spacecraft at a velocity greater than a few km s^{-1} the particle is instantly vaporized and heated to a high temperature, typically on the order of 10^4 to 10^5 K. At these high temperatures a substantial amount of the material is ionized, thereby producing a small expanding cloud of plasma. As the plasma cloud expands outward over the electric antenna, a voltage pulse is produced on the antenna. The exact details of the coupling of the plasma cloud to the antenna are somewhat uncertain. Laboratory measurements show that the total charge released by the impact is proportional to the mass of the impacting particle, i.e., $Q = km$, where k is a constant. For the Neptune flyby, where the impact speed is about 23 km s^{-1}, the yield constant, k, is estimated to be about 1.0 C g^{-1} (Gurnett et al. 1991; Pedersen et al. 1991). Usually it is assumed that the voltage pulse induced on the antenna is directly proportional to the total charge released. This proportionality can be written in the form

$$V = \alpha \frac{Q}{C_A} \tag{1}$$

where α is a dimensionless coupling constant, and C_A is the antenna capacity, which is $\sim$90 pF. In the above equation, note that α plays the role of an effective collection coefficient. Whether the antenna actually functions as a simple charge "collector" is, however, uncertain, because there are many other mechanisms for inducing a voltage change on the antenna. The best estimates for α come from comparisons with the planetary radio astronomy instrument. The radio astronomy instrument uses the electric antenna as a monopole, which simplifies the interpretation of the received signal (Aubier et al. 1983; Meyer-Vernet et al. 1986; Pedersen et al. 1991). For a monopole all of the charge released contributes to the voltage pulse, because the spacecraft itself acts as one element of the antenna (i.e., $\alpha = 1$ in Eq. [1]). Because the plasma-wave instrument responds to the difference in the voltage between the two antennas $\Delta V = V_1 - V_2$ (see Fig. 2), the response of the plasma wave instrument is inherently more complicated. Based on comparisons with the radio astronomy data, Gurnett et al. (1987) have estimated that the coupling constant for the plasma wave instrument is $\alpha = 4.8 \times 10^{-3}$. Inserting the appropriate constants into Eq. (1), the overall voltage response can be written

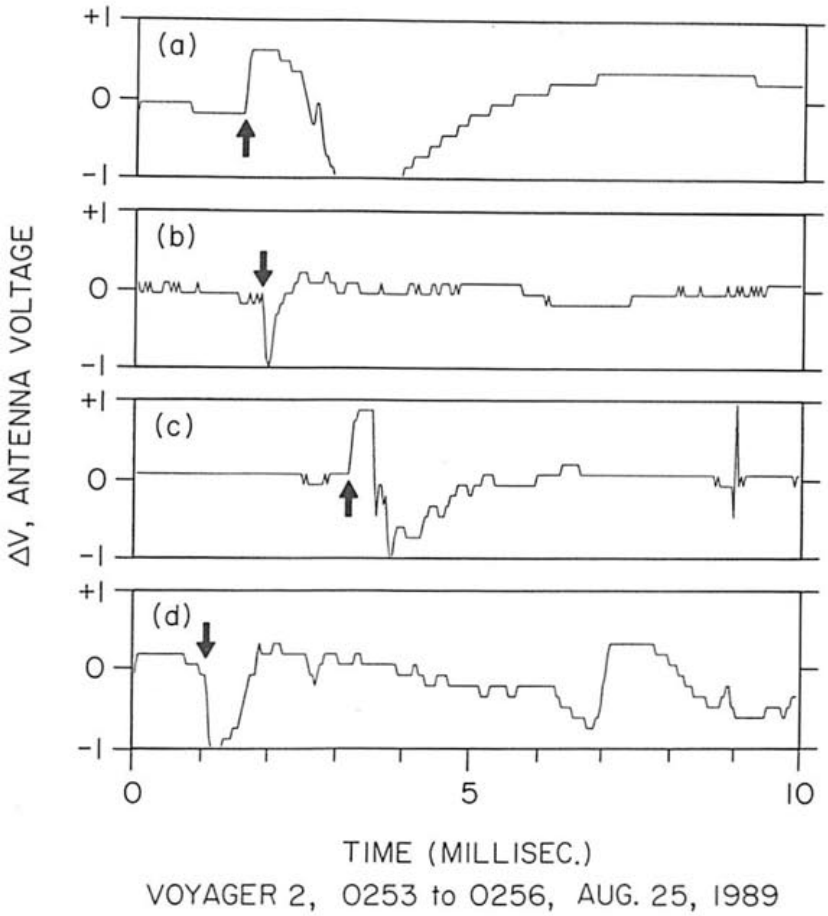

Figure 8. Some representative dust impact waveforms in the wideband waveform data. Dust impacts (indicated by the arrows) are followed by an abrupt pulse in the antenna potential. Both positive and negative pulses occur. The polarity is determined by the relative proximity of the impact to the two antenna elements (figure from Gurnett et al. 1991).

$V = (5.3 \times 10^7)m$, where V is the pulse height in volts, and m is the particle mass in grams.

The highest-resolution information on dust impacts comes from the wideband receiver, which provides direct measurements of the voltage waveform on the electric antenna. Some representative waveforms observed during the Neptune ring plane crossing are shown in Fig. 8. Typically the dust impact waveform consists of an abrupt voltage pulse followed by a complex recovery lasting from a fraction of one millisecond to several milliseconds. The rise time of the leading edge of the pulse is very fast, $\sim 30\,\mu$s. This rise time is essentially the response time of the anti-aliasing filter in the wideband receiver.

Both positive and negative polarity pulses are observed. The occurrence of both polarities is believed to be caused by the fact that the plasma-wave instrument responds to the difference in the potential between the two antenna elements. Thus, a particle striking one side of the spacecraft produces a polarity opposite to that of a particle striking the opposite side of the spacecraft (see Fig. 1). By counting the number of pulses, a detailed impact rate profile can be obtained. Figure 9 shows the impact rate profile for the inbound ring plane crossing, and Fig. 10 shows the outbound ring plane crossing. These impact rate profiles were determined by a computer algorthim that searches for an abrupt step in the antenna voltage with an amplitude exceeding a preset threshold. The distance Z at the top of these illustrations is the north-south distance (measured positive to the north) from the equatorial plane based on the spacecraft ephemeris. Each dot represents a measured impact rate, and the solid line is a multiparameter Gaussian fit to the impact rate profile. The asymmetric data coverage relative to the equatorial plane ($z = 0$) is due to constraints imposed on the use of the spacecraft tape recorder, which must also record high-priority imaging data during the same time period.

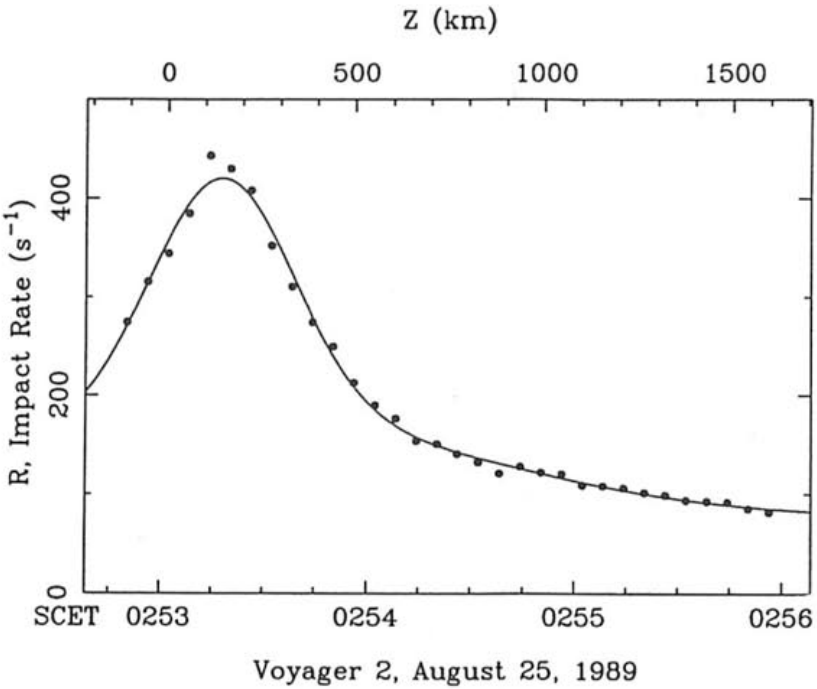

Figure 9. The impact rate profile (dots) obtained from the wideband data during the inbound equator crossing. The solid line is a multiparameter fit (two Gaussians). The center of the distribution is offset 146±4 km north (positive Z) of the equatorial plane (figure from Gurnett et al. 1991).

During the inbound ring plane crossing, the peak impact rate was $R = 443\ s^{-1}$, and during the outbound ring plane crossing the peak impact rate was $R = 151\ s^{-1}$. A small dead time ranging from one to several milliseconds is introduced after each impact due to saturation effects in the wideband receiver. The above impact rates were corrected for these dead time effects. The impact rates can be converted to number densities using the relation

$$R = nUA_{sc} \tag{2}$$

where n is the number density, U is the relative speed between the spacecraft and the particles, and A_{sc} is the effective area of the spacecraft body. The relative speed between the spacecraft and particles in circular prograde equatorial orbits was 23.6 km s^{-1} for the inbound ring plane crossing and 22.5 km s^{-1} for the outbound ring plane crossing. The effective cross-sectional area of the spacecraft, which does not count the high gain antenna because of its very low yield coefficient, has been computed by Gurnett et al. (1983*a*) and is $A_{sc} = 1.66\ m^2$. Using these nominal parameters, the peak number density is about $1.1 \times 10^{-2} m^{-3}$ for the inbound ring plane crossing, and $4.0 \times 10^{-3} m^{-3}$ for the outbound ring plane crossing.

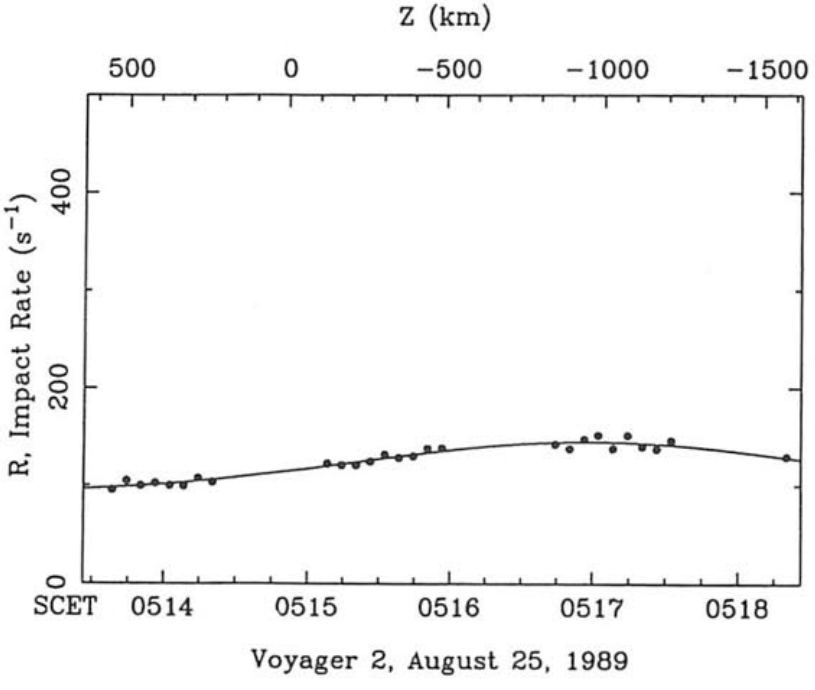

Figure 10. The impact rate profile (dots) obtained from the wideband data during the outbound equator crossing. The solid line is a Gaussian fit. The center of the distribution is offset 948±65 km south (negative Z) of the equatorial plane (figure from Gurnett et al. 1991).

The existence of two peaks in the dust impact rate, one near the inbound equator crossing and the other near the outbound equator crossing, strongly suggests that a dense disk of dust is circling the planet near the equatorial plane. As can be seen from Figs. 9 and 10, the locations of the maximum impact rates are not exactly at the equator ($z = 0$). For the inbound ring plane crossing, a Gaussian fit shows that the peak is shifted 146±4 km north of the equatorial plane, and for the outbound ring plane crossing the peak is shifted 948±65 km south of the equatorial plane. For a description of the Gaussian fit procedure, see Gurnett et al. (1991). The reversal in the position of the peak, from north to south, between the inbound and outbound equator crossings suggests that the plane of the disk is tilted relative to the equatorial plane. The tilt angle is roughly 0.4°. It should be noted that this interpretation is not necessarily unique, as radial variations cannot in principle be distinguished from north-south variations. Comparison of Figs. 9 and 10 clearly shows that the dust distribution is much broader on the outbound ring plane crossing than on the inbound ring plane crossing. This difference is probably related to the fact that the outbound ring plane crossing occurs farther from the planet than the inbound ring plane crossing (4.20 R_N vs 3.45 R_N). Assuming that the variations are primarily in the north-south direction, the half-thickness (Gaussian fit) of the disk is 268±11 km for the inbound crossing and 1036±196 km for the outbound crossing.

In addition to the dense "disk" of dust near the equatorial plane, a much more tenuous "halo" of dust also exists extending far away from the equatorial plane. Detailed examination of the wideband waveform data shows that impact rates of 1 to 10 particles per second are present over the entire region inside of 8 R_N, including the northern polar region (see Fig. 2). The lowest impact rate recorded in any of the wideband frames inside of 8 R_N is 0.6 s^{-1}.

By simultaneously measuring the rms antenna voltage, V_{rms}, and the impact rate, R, it is possible to estimate the rms mass of the impacting particles. Using the previously described assumptions regarding the linear coupling of the charge pulse to the antenna, it can be shown (Gurnett et al. 1991) that the rms mass of the impacting particles is given by

$$m_{rms} = \left(\frac{C_A}{\alpha k}\right) \frac{1}{(R\tau)^{1/2}} V_{rms} \tag{3}$$

where τ is the average duration of the voltage pulse. Unfortunately, the use of Eq. (3) has one difficulty, which is that R must be the impact rate of all the particles striking the spacecraft. Because the pulse identification algorithm has a threshold (set by the instrument noise level) below which impacts cannot be detected, the observed impact rate is always less that the true impact rate. Therefore, Eq. (3) rigorously gives only an upper limit to the rms mass. This limit is simply a recognition of the fact that a population of very small particles could exist that contributes to the rms voltage, but not to the counting rate. In practice, we doubt that such a population exists, because

a large number of very small particles should produce an intense "white noise" background that should be easily observed. As there is no evidence of such a background, it seems likely that most of the particles are being detected. Assuming that most of the particles are being counted, the rms mass can be estimated. Using the nominal parameters for the inbound ring plane crossing, $V_{rms}(\max) = 0.365$ volts, $R(\max) = 443\ s^{-1}$, and $\tau = 1$ ms, the rms mass works out to be 1.0×10^{-8} g. Similar results are obtained for the outbound ring plane crossing. Because of the large uncertainties in k and α, this estimate of the particle mass could very well be in error by up to a factor of 10. If we assume that the dust particles have a density of 1 g cm^{-3}, the particle radius works out to be 13.4 μm. Because this particle radius may be somewhat of an overestimate because of the factors described above, we conclude that a typical particle radius is probably on the order of 10 μm. This size estimate is similar to that obtained from the radio astronomy instrument (Pedersen et al. 1991).

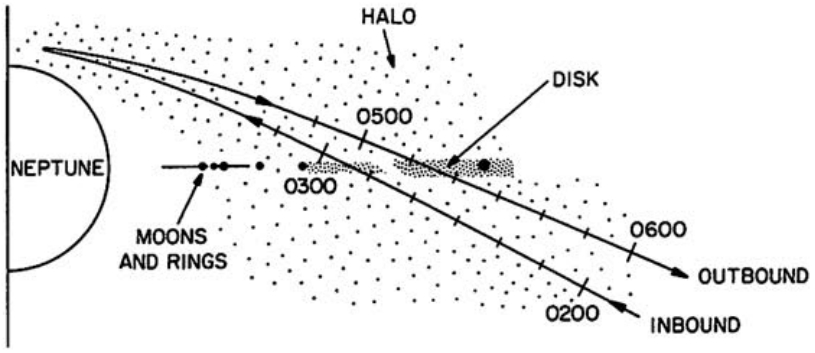

Figure 11. A meridian plane sketch of the spacecraft trajectory showing the dust distribution and its relationship to various moons and rings. The dust particles are believed to be produced by micrometeroid bombardment of satellites and large ring particles (figure from Gurnett et al. 1991).

It is generally believed (Burns et al. 1980,1984,1986; Morfill et al. 1980*a*, *b*) that small micron-sized particles in planetary ring systems are quickly destroyed on time scales of a few Myr. Because micron-sized particles cannot be of primordial origin, they must be continuously produced. The most likely source is believed to be micrometeoroid bombardment of satellites and larger ring particles. The Voyager imaging observations (Smith et al. 1989; Stone and Miner 1989) show that several small satellites and rings occur in the region where the dust impacts were observed. The locations of these satellites and rings are summarized in Fig. 11, which shows a plot of the Voyager trajectory in a meridian plane through the spacecraft. Also shown is a schematic representation of the dense "disk" of dust orbiting near the equatorial plane, and the much more tenuous "halo" of dust particles extending well away from the equator. The satellites and rings provide suitable

sources for the particles orbiting near the equatorial plane. However, they cannot account for the "halo" particles, because large energies are required to inject particles into highly inclined orbits. Electromagnetic interactions with the planetary magnetic field are believed to be the primary mechanism for achieving these high inclinations. Small dust particles are charged by photoemission and electron collection from the surrounding plasma. Early studies by Northrop and Hill (1983), Schaffer and Burns (1987), and others showed that the Lorentz force, $q(\mathbf{E} + \mathbf{V} \times \mathbf{B})$, can cause significant orbital perturbations, particularly if the particles are in the micron-size range and smaller. D. P. Hamilton (personal communication) has carried out computer simulations of dust particle orbits at Neptune using an offset tilted magnetic field. His simulations show that micron-sized particles orbiting near the equatorial plane can be perturbed into highly inclined orbits on time scales of a few million years or less. This mechanism is particularly effective when the Keplerian orbit motion is in resonance with the rotating magnetic field of the planet. Although no attempt has yet been made to account for the detailed spatial distribution of the "halo" particles, it seems reasonably certain that electromagnetic interactions play an important role in the dynamics of these particles.

The apparent tilt of the dust disk, as indicated by the reversal in the centroid of the north-south dust distribution between the inbound and outbound passes, has not received a detailed analysis. The most likely possibility (P. Nicholson, personal communication, 1989) is that this tilt is a gravitational perturbation effect caused by Neptune's moon, Triton, whose orbit is inclined at a substantial angle (22.3°) relative to Neptune's equatorial plane.

V. WHISTLERS

During the pass through the inner region of the magnetosphere several highly dispersed narrowband signals were detected that are believed to be whistlers generated by atmospheric lightning. Terrestrial whistlers were first discovered by Barkhausen (1919) using a groundbased very low-frequency radio receiver. When played through a loudspeaker the signals consist of whistling tones, usually decreasing in frequency with increasing time, hence the term "whistler." Eckersley (1935) first suggested that these signals are produced by lightning, and Storey first explained their propagation through the Earth's magnetosphere via a mode of propagation now known as the whistler mode (Stix 1962). As currently understood these signals propagate more or less along the magnetic field at frequencies below the electron cyclotron frequency or electron plasma frequency, whichever is smaller. The whistling character of the signal is due to the frequency dependence of the index of refraction, which causes the impulsive energy of the lightning discharge to be dispersed into a whistling tone. At frequencies well below the electron cyclotron frequency, $f << f_{ce}$, and in a sufficiently dense plasma, $f_{pe}^2 >> f\, f_{ce}$, the travel time at frequency f varies as $t = D/\sqrt{f}$, where D is a quantity called the

dispersion. The above dispersion equation is often called the Eckersley law, after Eckersley (1935) who first discovered the relationship. Often whistlers bounce back and forth from one hemisphere to another along the same magnetic field line, forming a series of tones known as a whistler train. For an overview of terrestrial whistler observations and the associated theory, see Helliwell (1965). In addition to the terrestrial observations, whistlers have also been observed at Jupiter (Scarf et al. 1979*b*; Gurnett et al. 1979), and possibly at Venus (Taylor et al. 1979; Scarf et al. 1980; Taylor and Cloutier 1986).

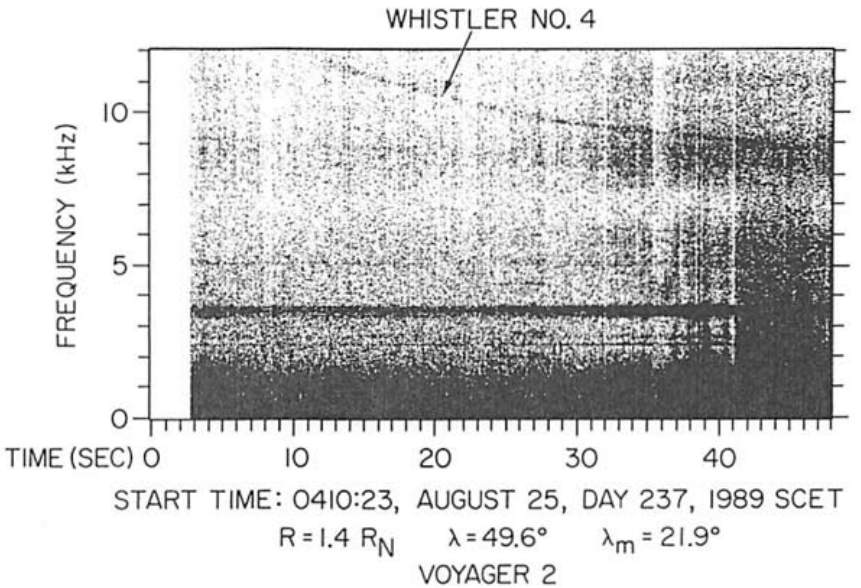

Figure 12. A wideband frequency-time spectrogram showing a whistler that was detected in the inner region of the magnetosphere shortly after closest approach. This was the fourth of sixteen whistlers that were detected during the flyby (figure from Gurnett et al. 1990).

An example of a whistler detected by Voyager 2 at Neptune is shown in Fig. 12. This spectrogram is from a wideband frame obtained at $\sim 1.44\,R_N$, shortly after closest approach. The identifying characteristic of a whistler, consisting of a narrowband tone decreasing in frequency with increasing time, is clearly evident. When the plasma-wave observations from Neptune were first reported by Gurnett et al. (1989), because of the extremely large dispersions, it was not certain that these signals were in fact whistlers. However, in a subsequent study Gurnett et al. (1990) confirmed that the dispersion fits the Eckersley law, which provides strong evidence that the signals are in fact whistlers. A total of 16 whistlers were observed at Neptune. All 16 events occurred close to the planet, at radial distances ranging from 1.30 to $1.99\,R_N$,

and at low magnetic latitudes, $-7° < \lambda_m < 33°$. A plot giving the location of these events as a function of radial distance and magnetic latitude is shown in Fig. 13. The most striking feature of the whistlers at Neptune is the extremely large dispersion. The D values, from the Eckersley dispersion law, varied from 24,330 s $Hz^{1/2}$ to 45,462 s $Hz^{1/2}$, with most of the values clustered in a narrow range around 26,000 s $Hz^{1/2}$. These dispersions are much larger than the dispersion of single hop terrestrial whistlers, which range from about 12 to 200 s $Hz^{1/2}$ (Helliwell 1965), and are also large compared to the dispersion of Jovian whistlers, which range from 45 to 500 s $Hz^{1/2}$ (Kurth et al. 1985).

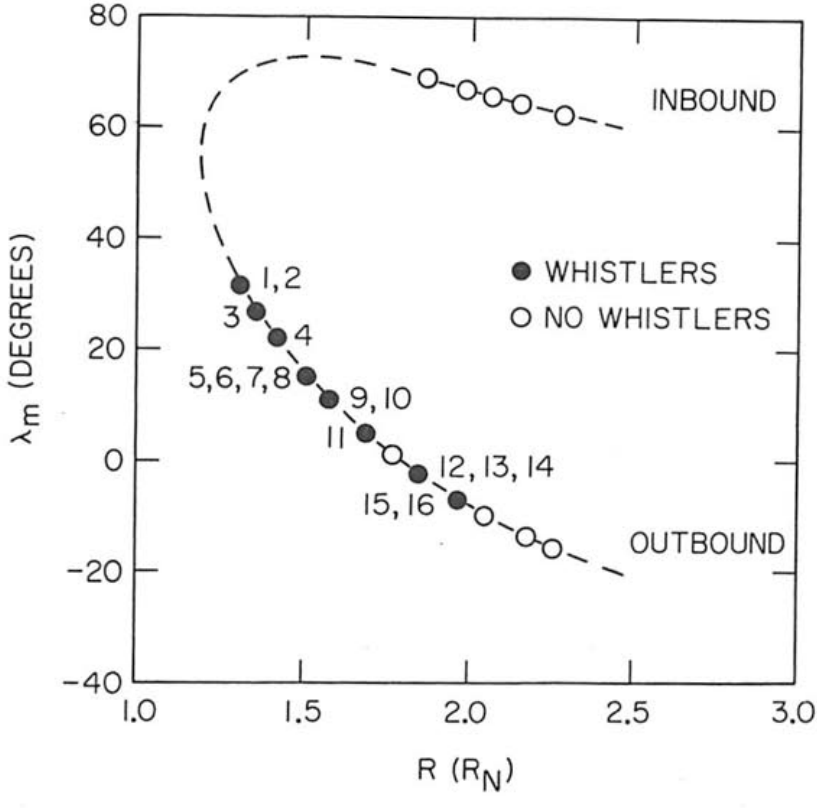

Figure 13. A radial distance, R, magnetic latitude, λ_m, plot of the spacecraft trajectory showing the location of all the observed whistlers. The solid black dots are wideband frames with whistlers, and the open circles are wideband frames with no whistlers (figure from Gurnett et al. 1990).

Whistlers place important constraints on the plasma density in Neptune's magnetosphere. For whistlers to propagate, both the electron cyclotron frequency and electron plasma frequency must be greater than the wave frequency at all points along the propagation path. Most of the whistlers observed

had frequencies extending up to ~12 kHz, which is the upper frequency limit of the wideband receiver. Based on the OTD2 magnetic field model of Ness et al. (1989), the constraint $f_{ce} > 12$ kHz implies that the ray path cannot extend to radial distance $\gtrsim 3\ R_N$. Because the ray path of whistlers can make an angle of as much as 19° relative to the magnetic field (Storey 1953), it is difficult to make a precise statement about the ray path, other than to state that it is more or less along the magnetic field line. No evidence exists for whistler trains, so it would appear that the signals are all due to single-hop ray paths. One whistler has roughly twice the dispersion of the remaining whistlers, so it is possible that this signal could be due to a two-hop ray path. The constraint $f_{pe} > 12$ kHz rigorously limits the electron density to no less than 1.8 cm^{-3} at all points along the ray path. The fact that the travel time fits the Eckersley law, which is only valid if $f_{pe}^2 >> f\ f_c$, implies that the electron densities must be even higher, probably 30 to 100 cm^{-3}, otherwise the travel time vs frequency plot would have the form of a "nose whistler" (see Helliwell 1965). These densities are considerably higher than those obtained by the Voyager plasma instrument (Belcher et al. 1989), which gave maximum ion densities in the region near closest approach of either 0.6 or 1.4 cm^{-3}, depending on whether H^+ or N^+ is assumed to be the dominant ion. The prevailing view (R. L. McNutt, personal communication) is that if the plasma is very cold, i.e., <1000 K, then the cold component would not have been detected by the plasma instrument, which was oriented to search for precipitating auroral particles during the period when the whistlers were observed. Electron density measurements were also obtained in Neptune's ionosphere from the radio science investigation (Tyler et al. 1989). These measurements indicated a peak electron density of $\sim 2 \times 10^3$ cm^{-3} at an altitude of ~1400 km, decreasing with increasing altitude with a scale height of ~1800±300 km. The ionosphere is very cold, with a temperature of about 950±160 K, assuming H^+ to be the dominant ion. Reliable density measurements can only be obtained at altitudes up to ~5000 km, at which point the electron density has declined to on the order of a few hundred cm^{-3}. Unfortunately, the radio science electron density measurements are only applicable to the region near the terminator, and cannot be directly compared to the region sampled by Voyager, except in very general terms.

Further information on the plasma density can be obtained from the dispersion of the whistlers. For terrestrial whistlers the dispersion D in the Eckersley law is often calculated using the relation

$$D = \frac{1}{2c} \int \frac{f_{pe}}{\sqrt{f_{ce}}} ds \tag{4}$$

where c is the speed of light, and the integral is evaluated along the ray path of the whistler. The derivation of Eq. (4) involves a number of assumptions, the main one being that the ray path must be approximately parallel to the magnetic field line (i.e., small wave normal angles). Although Eq. (4) works well for

most whistler propagation in the Earth's magnetosphere, attempts to use this relation at Neptune quickly revealed that unreasonably long propagation paths and/or large plasma densities are required to explain the observed dispersions. For a discussion of these difficulties, see Gurnett et al. (1990). Subsequent investigations by Menietti et al. (1991) using a computer ray tracing code, which is not restricted to the quasi-parallel assumption implicit in Eq. (4), have apparently resolved this issue. It is found that as the whistler signal propagates into the low density regions of Neptune's magnetosphere, the wave normal angle quickly approaches the resonance cone angle (Stix 1962), where the index of refraction goes to infinity. In the vicinity of the resonance cone, the group velocity becomes small relative to parallel propagation, thereby greatly increasing the travel time and dispersion. Ray path calculations using representative magnetospheric plasma density models, which are necessarily highly uncertain, have been able to account for dispersions comparable to those observed.

One final issue concerning the whistler observations at Neptune is the fact that few if any impulsive lightning signals were detected by the planetary radio astronomy instrument (Warwick et al. 1989). Kaiser et al. (1991) have investigated this problem and have concluded that the observations from the planetary radio astronomy instrument do not preclude the possibility of atmospheric lightning. Careful examination of the radio astronomy data has in fact led to the identification of four possible lightning events. However, these events are very weak and Kaiser et al. are hesitant to definitely claim that they are due to lightning. In any case, it is clear that the lightning-related signals are very weak compared to those observed at Saturn (Kaiser et al. 1983) and Uranus (Zarka and Pedersen 1986). Even the absence of definitive high-frequency radio signals from lightning is not necessarily inconsistent with the whistler observations. As pointed out by Gurnett et al. (1990), the whistler signals are extremely weak, even weaker than terrestrial lightning at a comparable distance from the planet. The peak broadband electric field strength of the whistler signals in Fig. 12, for example, is estimated to be only $\sim 12\,\mu\mathrm{V\ m^{-1}}$. Given the expected radio emission spectrum of lightning, which decreases as $1/f^2$ (Pierce 1977), this field strength translates to only $0.01\,\mu\mathrm{V\ m^{-1}}$ at 10 MHz, which is where the radio astronomy measurements are made. Even given the uncertainties concerning the refractive index, the range to the source, and the propagation path, this signal is much too weak to be detected by the Voyager radio astronomy instrument. For a further discussion of lightning observations from the PRA instrument, see the Chapter by Zarka et al.

VI. PLASMA-WAVE EMISSIONS IN THE INNER MAGNETOSPHERE

The interpretation of the emissions that exist in the inner magnetosphere is complicated by two factors. First, the low intensities make it very difficult to

identify characteristic cutoffs and resonances that can be used to determine the mode of propagation. Second, because the plasma instrument cannot detect the cold component of the plasma in the region near closest approach, the electron plasma frequency, which is a crucial parameter for mode identification, is almost completely unknown. One notable feature of the observations in the inner magnetosphere is the absence of intense whistler-mode chorus and hiss emissions. Whistler-mode emissions are driven by the loss cone in the trapped radiation belt electrons (Kennel and Petschek 1966), and are a common feature of the radiation belts of Earth (Helliwell 1965), Jupiter (Scarf et al. 1979*b*), Saturn (Gurnett et al. 1981*a*) and Uranus (Gurnett et al. 1986). Because the radiation-belt electron intensities at Neptune are lower than at other planetary magnetospheres (Krimigis et al. 1989), it is possible that strong whistler-mode emissions are simply not excited in the magnetosphere of Neptune. The absence of whistler-mode emissions from radiation-belt electrons may also be due to the unusual trajectory through the magnetic field of Neptune. Because of the large tilt of the magnetic dipole axis and the time of arrival relative to the planetary rotation, the spacecraft did not provide good coverage of the magnetic equatorial region inside of $\sim 5\,R_N$. Because the most intense whistler-mode emissions usually occur near the magnetic equator, it is possible that the spacecraft did not sample the proper region of the magnetosphere to detect these emissions.

To interpret the emissions that do exist in the inner magnetosphere, it is first necessary to discuss the electron plasma frequency. The primary method of obtaining information on the electron plasma frequency is from resonances and cutoffs in the plasma-wave spectrum. The interpretation of cutoffs and resonances requires an implicit assumption about the plasma-wave mode involved, and a later check to see if the derived electron plasma frequency is consistent with all of the known facts. Using this approach, Gurnett et al. (1990) have placed upper and lower bounds on the electron plasma frequency profile in the region around closest approach. Their results are summarized in Fig. 14. The upper panel of Fig. 14 shows the inferred limits on the electron plasma frequency (hence, electron density), and the lower panel shows the plasma-wave emissions that were used to establish these limits. To aid in the interpretation, the electron cyclotron frequency, f_{ce}, computed from the magnetic field data (provided by N. F. Ness) is shown in the top panel. Starting from the left, an upper bound to the electron plasma frequency, $f_{pe}(\max)$, is obtained from the low-frequency cutoff of the emission band that can be seen extending below the electron cyclotron frequency from ~0300 to 0352 SCET. This emission is believed to be either free space L-O mode radiation, or trapped Z-mode radiation. Of the two, the low-frequency cutoff of the Z-mode radiation gives the upper bound on the plasma frequency. This cutoff ($f_{L=0}$) is related to the plasma frequency via the equation $f_{L=0} = -f_{ce}/2 + [(f_{ce}/2)^2 + f_{pe}^2]^{1/2}$. In the period from ~0405 to 0425 SCET, the upper frequency limit of the whistlers described in the previous section provides a lower limit to the electron plasma frequency.

identify characteristic cutoffs and resonances that can be used to determine the mode of propagation. Second, because the plasma instrument cannot detect the cold component of the plasma in the region near closest approach, the electron plasma frequency, which is a crucial parameter for mode identification, is almost completely unknown. One notable feature of the observations in the inner magnetosphere is the absence of intense whistler-mode chorus and hiss emissions. Whistler-mode emissions are driven by the loss cone in the trapped radiation belt electrons (Kennel and Petschek 1966), and are a common feature of the radiation belts of Earth (Helliwell 1965), Jupiter (Scarf et al. 1979*b*), Saturn (Gurnett et al. 1981*a*) and Uranus (Gurnett et al. 1986). Because the radiation-belt electron intensities at Neptune are lower than at other planetary magnetospheres (Krimigis et al. 1989), it is possible that strong whistler-mode emissions are simply not excited in the magnetosphere of Neptune. The absence of whistler-mode emissions from radiation-belt electrons may also be due to the unusual trajectory through the magnetic field of Neptune. Because of the large tilt of the magnetic dipole axis and the time of arrival relative to the planetary rotation, the spacecraft did not provide good coverage of the magnetic equatorial region inside of $\sim 5\,R_N$. Because the most intense whistler-mode emissions usually occur near the magnetic equator, it is possible that the spacecraft did not sample the proper region of the magnetosphere to detect these emissions.

To interpret the emissions that do exist in the inner magnetosphere, it is first necessary to discuss the electron plasma frequency. The primary method of obtaining information on the electron plasma frequency is from resonances and cutoffs in the plasma-wave spectrum. The interpretation of cutoffs and resonances requires an implicit assumption about the plasma-wave mode involved, and a later check to see if the derived electron plasma frequency is consistent with all of the known facts. Using this approach, Gurnett et al. (1990) have placed upper and lower bounds on the electron plasma frequency profile in the region around closest approach. Their results are summarized in Fig. 14. The upper panel of Fig. 14 shows the inferred limits on the electron plasma frequency (hence, electron density), and the lower panel shows the plasma-wave emissions that were used to establish these limits. To aid in the interpretation, the electron cyclotron frequency, f_{ce}, computed from the magnetic field data (provided by N. F. Ness) is shown in the top panel. Starting from the left, an upper bound to the electron plasma frequency, $f_{pe}(\max)$, is obtained from the low-frequency cutoff of the emission band that can be seen extending below the electron cyclotron frequency from ~0300 to 0352 SCET. This emission is believed to be either free space L-O mode radiation, or trapped Z-mode radiation. Of the two, the low-frequency cutoff of the Z-mode radiation gives the upper bound on the plasma frequency. This cutoff ($f_{L=0}$) is related to the plasma frequency via the equation $f_{L=0} = -f_{ce}/2 + [(f_{ce}/2)^2 + f_{pe}^2]^{1/2}$. In the period from ~0405 to 0425 SCET, the upper frequency limit of the whistlers described in the previous section provides a lower limit to the electron plasma frequency.

The frequency range in which the whistlers occur is shown schematically by the whistler symbols in the upper panel of Fig. 14. During this same general period, from ~0358 to 0420 SCET, a weak band of noise can be seen in the bottom panel of Fig. 14, extending up to a frequency of ~50 kHz. As this noise occurs in the same general frequency range as the whistlers, it is also most likely propagating in the whistler mode. The upper frequency limit of the whistler-mode noise places a lower limit on the electron plasma frequency (recall that the whistler mode cannot propagate if $f > f_{pe}$). This lower limit is labeled f_{pe}(min) in Fig. 14. At 0420 SCET, almost exactly at the magnetic equator crossing, Sawyer et al. (1990) reported a narrow, well-defined burst of waves in the frequency range from 104 to 212 kHz, slightly above the electron cyclotron frequency. These waves appear to be low order $(n + 1/2)f_{ce}$ electron cyclotron harmonic waves, very similar to the electron cyclotron harmonic waves described earlier at the inbound and outbound magnetic equator crossings. The frequency range of these waves is indicated by the arrow labeled "$(n + 1/2)f_{ce}$" in Fig. 14. Electron cyclotron harmonic waves are very difficult to generate unless the electron plasma frequency is near or above the wave frequency, which implies that $f_{pe} \gtrsim 212$ kHz. An electron plasma frequency of 212 kHz would correspond to an electron density of 500 cm^{-3}. Shortly afterwards, from ~0423 to 0515 SCET, a band of noise can be seen in the bottom panel of Fig. 14 from ~6 to 30 kHz. As on the inbound pass, this noise can be interpreted as either free space L-O mode radiation or Z-mode radiation (Kurth et al. 1990). Assuming that the low-frequency cutoff of this noise is at $f_{L=0}$, as was done on the inbound pass, one obtains an upper limit to the electron plasma frequency, labeled f_{pe}(max) in the top panel of Fig. 14. To complete the analysis, a lower limit to the electron density can be obtained from the PLS plasma density measurements (Richardson et al. 1991; data obtained via the Planetary Data System). This limit is shown by the solid line labeled PLS near the bottom of the upper panel in Fig. 14. The break in this line near closest approach, from ~0343 to 0410 SCET, corresponds to a region where no density measurements were available from PLS because the signal was below the instrument noise level (J. Richardson, personal communication). Combining all of these limits then defines a region within which the electron plasma frequency must be located. This region is indicated by the dotted shading in Fig. 14. From this analysis it appears that the electron plasma frequency was in the range from ~3 to 10 kHz (0.1 to 1 electron cm^{-3}) on the inbound pass, rose rapidly at ~0340 SCET, reached a peak of at least 30 to 200 kHz (11 to 500 electrons cm^{-3}) shortly after closest approach, dropped abruptly at ~0425 SCET, and returned to about 3 to 10 kHz (0.1 to 1 electron cm^{-3}) on the outbound pass. The enhanced electron density in the region near closest approach is probably caused by the passage of the spacecraft through a cold dense ionospheric plasma, possibly similar to that detected by the radio occultation experiment near the limb of the planet (Tyler et al. 1989).

Not all of the plasma-wave emissions detected in the inner regions of the

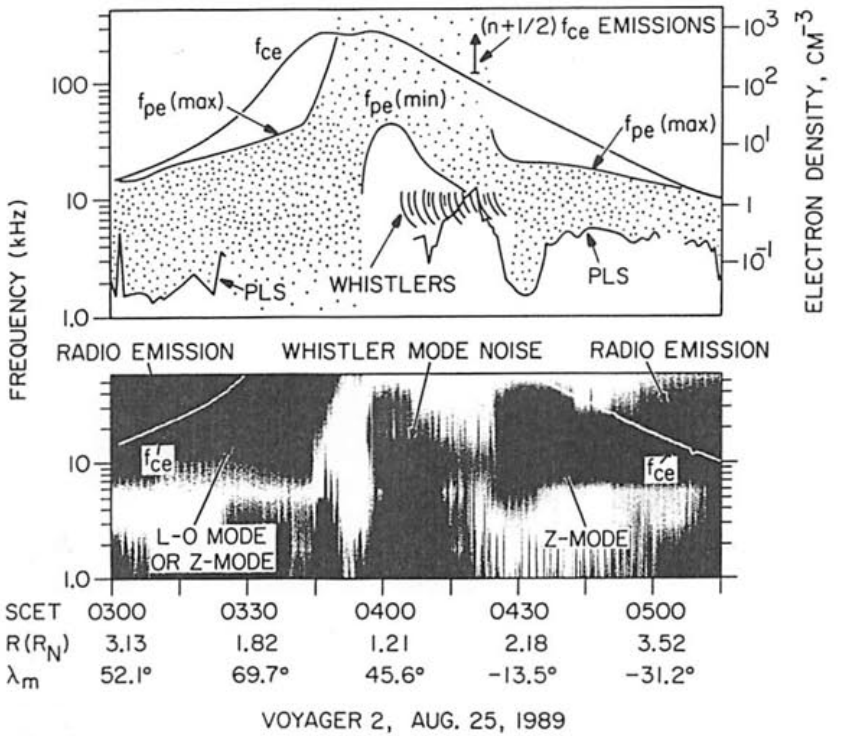

Figure 14. The top panel shows the limits that can be placed on the electron plasma frequency (to the left) and electron density (to the right) from various plasma-wave cutoffs and resonances, and from the plasma instrument. The electron density must lie in the region indicated by the dotted shading. The bottom panel shows the frequency-time spectrogram that was used to derive f_{pe} (max) and f_{pe} (min) (figure after Gurnett et al. 1990).

magnetosphere are easy to interpret. One of the most difficult is a narrowband emission that varies from 3.0 to 4.3 kHz over the period from 0310 to 0538 SCET. This emission is very weak, $\sim 10\,\mu\mathrm{Vm}^{-1}$, and can only be clearly identified in the wideband data. Figure 15 shows a mosaic of 12 wideband spectrograms in which this emission can be clearly seen. The most notable characteristic of this emission is the nearly constant frequency. The constancy of the frequency is particularly difficult to explain, because the magnetic field strength, and most likely the electron density, vary substantially in the region where the emission is observed. The emission frequency, below the electron cyclotron frequency, is in a suitable range for the whistler mode. However, it is very hard to understand how a whistler-mode generation mechanism could lead to such a constant frequency over such a large spatial region. Because whistler-mode emissions tend to propagate along the magnetic field lines, the emission frequency would be expected to vary significantly from one L-shell to the next. For a recent analysis supporting the view that these waves were

caused by whistler-mode emissions see Sonwalkar et al. (1995). Somewhat similar narrowband emissions were also observed at Saturn (Gurnett et al. 1981*b*). At Saturn a strong case can be made that the narrowband signals are radio emissions propagating in the free-space *L-O* mode. If we assume that the narrowband emissions in Fig. 15 are propagating in the free space *L-O* mode, then it follows that the electron plasma frequency must be below ~3 kHz over the entire frequency where these emissions were observed, because the *L-O* mode cannot propagate at frequencies below the electron plasma frequency. Such a low plasma frequency is inconsistent with the whistler observations, which require that the electron plasma frequency must be well above 10 kHz. Thus, it appears that the narrowband emissions cannot be propagating in the free space *L-O* mode.

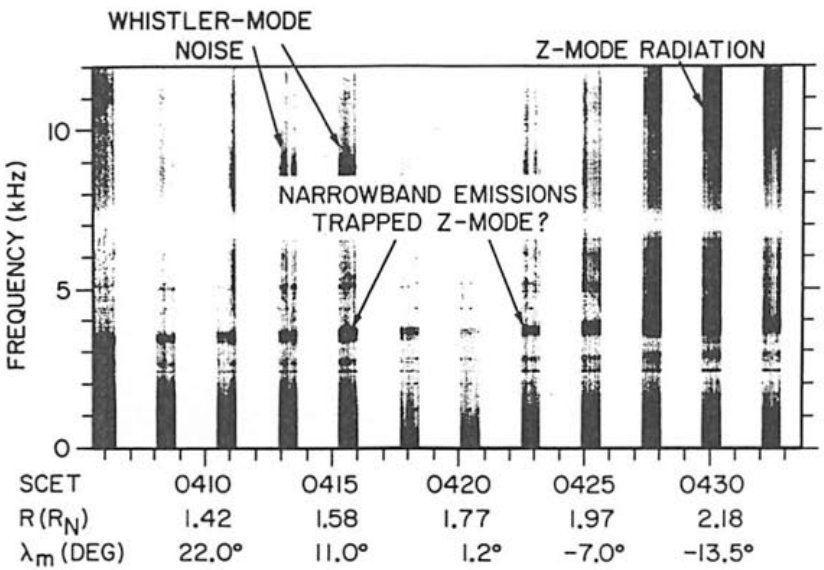

Figure 15. A series of wideband spectrograms showing the narrowband emissions observed near closest approach. These emissions are believed to be produced either by whistler-mode emissions or by Z-mode radiation trapped within the magnetospheric cavity (figure adapted from Moses and Coroniti 1991).

Moses and Coroniti (1991) have carried out a detailed study of the narrowband emissions and have suggested that the emissions are propagating in the Z mode. If the electron plasma frequency is well below the electron cyclotron frequency, the Z mode has many features similar to the free space *L-O* mode. In particular, over a large frequency range, from $f_{L=0}$ to near f_{ce}, the mode is nearly isotropic, which allows the radiation to propagate over large regions with very little refraction. This ability to propagate with little or no refraction provides a plausible explanation for the nearly constant frequency,

as the spacecraft could be simply receiving radiation from a distant source. Although the Z-mode radiation can propagate long distances, the radiation nevertheless cannot escape from the plasma. For this reason Moses and Coroniti (1991) refer to the narrowband emissions as "trapped Z-mode" radiation. Similar observations of trapped Z-mode radiation have been reported in the Earth's magnetosphere (Gurnett et al. 1983*b*).

Because the trapped Z-mode interpretation of the narrowband emission requires that the $f_{L=0}$ cutoff frequency remain below the emission frequency, this constraint puts an upper limit on the electron plasma frequency via the equation $f_{L=0} = -f_{ce}/2 + [(f_{ce}/2)^2 + f_p^2]^{1/2}$. In most respects this constraint is consistent with the limits on the electron density shown in Fig. 14. The most serious inconsistency concerns the $(n + 1/2)f_{ce}$ electron cyclotron harmonics emissions at 0420 SCET. As discussed earlier, the existence of the electron cyclotron harmonics implies that the electron density is quite high, roughly 500 cm^{-3} or higher, at this time. The maximum electron density permitted by the trapped Z-mode interpretation is 4.8 cm^{-3} (Moses and Coroniti 1991). Whether this inconsistency can be reconciled remains to be seen. One possibility is that the waves identified as $(n + 1/2)f_{ce}$ emissions could be remotely generated radio emissions instead of electron cyclotron waves. Another possibility is that perhaps the electron cyclotron waves can be generated at electron densities below 500 cm^{-3}. Further study is needed to determine if this is possible. Finally, it should be mentioned that the electron density implied by the trapped Z-mode interpretation provides an uncomfortable, but not impossible constraint on the propagation of whistlers. For example, the last whistler observed, at 0425:30 SCET, has an upper frequency limit of 12.0 kHz (Gurnett et al. 1990). The upper limit to the electron plasma frequency given at this time by the trapped Z-mode interpretation is 17.8 kHz (Moses and Coroniti 1991). Although these frequencies satisfy the $f < f_{pe}$ requirement for the propagation of whistlers, it is difficult to avoid a "nose" in the whistler dispersion curve, which is not observed.

As can be seen in Fig. 15, an enhanced band of noise exists at low frequencies near the bottom of the spectrogram. This noise is believed to be caused by emissions near low-order harmonics of the proton cyclotron frequency (Barbosa et al. 1990). The spectrum of this noise can be seen more clearly in Fig. 16, which shows a 1-hr frequency-time spectrogram generated from the low-rate data in the region shortly after closest approach. The white line labeled f_{cp} is the proton cyclotron frequency, which was computed from magnetic field data provided by N. F. Ness. As can be seen, a well-defined band of noise exists slightly above the proton cyclotron frequency. This noise becomes particularly intense and broadens upward in frequency around 0420 SCET, near the magnetic equator.

Waves slightly above the proton cyclotron frequency near the magnetic equator are a common feature of planetary magnetospheres. In the Earth's magnetosphere equatorial waves of this type were first discovered by Russell et al. (1970). Later studies by Gurnett (1976), Olsen (1981), Perraut et al.

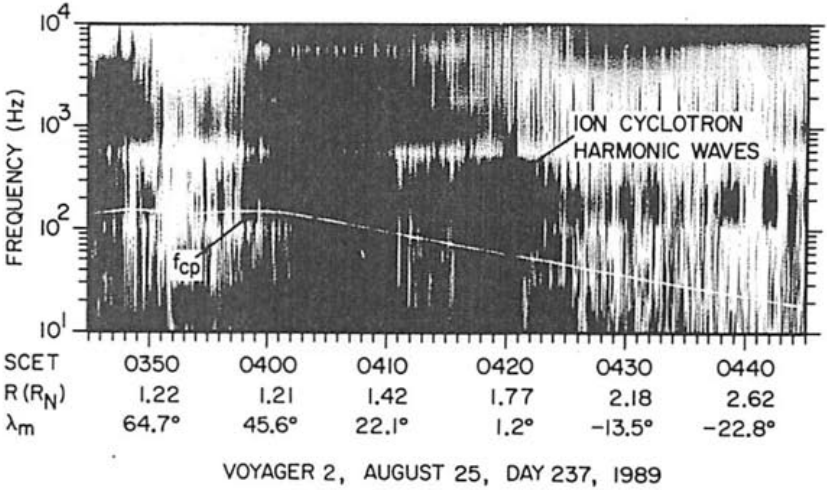

Figure 16. A frequency-time spectrogram showing the enhanced noise levels observed near and slightly above the proton cyclotron frequency, f_{cp}. These waves are believed to be ion Bernstein waves. Electromagnetic ion cyclotron waves may also be present below the proton cyclotron frequency from ~0400 to 0411 SCET (figure adapted from Barbosa et al. 1990).

(1982), Olsen et al. (1987), and Boardsen et al. (1991) showed that the waves are associated with harmonics of the ion cyclotron frequency and are driven by highly anisotropic 20 to 50 eV ions trapped near the magnetic equatorial plane. Polarization measurements show that the waves have both electric and magnetic field components (i.e., an electromagnetic wave), and that the wave vector is oriented nearly perpendicular to the magnetic field. These properties identify the mode of propagation as the magnetosonic mode (Perraut et al. 1982). This mode is essentially the same as the whistler mode, but thermal effects are included in the dispersion relation. Somewhat similar waves have been identified by Barbosa and Kurth (1990) in the cold ion torus at Jupiter near harmonics of the proton cyclotron frequency. However, in contrast to the terrestrial observations, Barbosa and Kurth interpret these waves as electrostatic ion Bernstein waves. Because charge-exchange ionization in the rapidly rotating Io torus is expected to produce highly unstable ring-type ion distributions, they argue that electrostatic waves (ion Bernstein modes) are more likely to be excited than electromagnetic waves (magnetosonic mode). Because no wave magnetic field measurements were available at Jupiter, the electrostatic/electromagnetic character of the emission could not be determined.

The waves observed slightly above the proton cyclotron frequency at Neptune are interpreted by Barbosa et al. (1990) as electrostatic ion Bernstein waves driven by pick-up ions, very similar to the interpretation of the ion cyclotron harmonic emissions in the Io torus. The neutral atoms involved

in the ion pick-up process are believed to be nitrogen that originates from Triton's exosphere. These atoms are believed to be ionized near Triton's orbit, and then diffused into the inner regions of the magnetosphere. As the particles diffuse inward they gain energy by adiabatic acceleration, thereby producing the hot ring-like distribution required to excite ion Bernstein waves. The ion heating involved in this inward diffusion is believed to be adequate to explain the hot ion distributions observed by the PLS instrument in the region where the waves were observed. As with the Jupiter observations, no wave magnetic field measurements are available to confirm that the waves are in fact electrostatic. For this reason, one cannot rule out the possibility that the waves might be propagating in the magnetosonic mode.

Enhanced electric field intensities can also be seen in Fig. 16 at frequencies below the proton cyclotron frequency from ~0400 to 0411 SCET. In the initial presentation of the Neptune observations, Gurnett et al. (1989) suggested that these waves may be electromagnetic ion cyclotron waves. Since then no further work has been done on the origin of these emissions. Detailed analysis of these emissions is complicated to some extent by the very low intensities, and the high level of dust impact noise that occurs in this part of the spectrum.

VII. SUMMARY AND CONCLUSION

The Voyager 2 plasma wave investigation provided valuable data on a wide variety of phenomena at Neptune. During the approach to the planet, upstream electron plasma oscillations provided the first evidence of the approach to the bow shock. A strong burst of electrostatic noise signaled the crossing of the bow shock. Within the magnetosphere electrostatic waves at low-order half-integral harmonics of the electron cyclotron frequency and at the upper hybrid resonance were observed at both the inbound and outbound magnetic equator crossings. These electrostatic waves are believed to be responsible for the low-frequency continuum radiation escaping from the planet at frequencies $\gtrsim$5 kHz, and may play a role in the pitch-angle scattering of low-energy electrons. The dust impact data show that the dust distribution consists of a dense "disk" of dust orbiting near the equatorial plane, and a tenuous "halo" extending far from the equatorial plane, including the region over the north pole. The peak impact rates at the equator crossings were 443 s^{-1} and 151 s^{-1}, corresponding to number densities of 1.1×10^{-2} and 4.0×10^{-3} m^{-3}, respectively. Using the best available models for the coupling of the dust impact signal to the electric antennas, the rms mass of the impacting particles is estimated to be $\sim 10^{-8}$ g. For water ice the corresponding radius of these particles is on the order of 10 μm.

During the pass through the inner magnetosphere, 16 highly dispersed narrowband signals were observed that are believed to be whistlers produced by atmospheric lightning. The dispersion of these signals is very large, ~24,000 to 45,000 s $Hz^{1/2}$, much larger than at any other planet. The large dis-

persion is believed to be caused by propagation at wave normal angles very close to the resonance cone where the group velocity becomes very small. Several other types of naturally generated plasma-wave emissions were also observed in the inner region of the magnetosphere, all of which were very weak. One of the most unusual was a narrowband emission at a frequency of ~3.0 to 4.3 kHz. The current interpretation of this emission is that it is either whistler-mode radiation or trapped Z-mode radiation originating from a remote source, the details of which are unknown. Analysis of the cutoff frequencies of various emissions observed in the inner magnetosphere provides limits on the electron density. These limits indicate that the spacecraft passed through a region of cold dense ionospheric plasma near closest approach, with densities of at least 30 cm^{-3}, and possibly as high as 500 cm^{-3}. A band of low-frequency electric field noise was also observed near the magnetic equator at frequencies slightly above the proton cyclotron frequency. This noise is believed to be caused by electrostatic ion Bernstein waves excited by pick-up ions. The pick-up ions are believed to have originated from charge exchange interactions between the rapidly rotating magnetospheric plasma and nitrogen escaping from the atmosphere of Triton.

Although a good overall understanding of the plasma-wave phenomena observed at Neptune has been achieved, various details remain poorly understood. Because of the complexity of the processes involved, considerable uncertainty still exists concerning the coupling of the dust impact signal to the electric antenna. These uncertainties do not affect the impact rate profiles, but do affect the estimated mass of the impacting particles, possibly by factors of 10 or more. Within the inner magnetosphere the details of the electron density profile remain uncertain, in part due to difficulties in clearly identifying the mode of propagation of certain emissions, such as the 3.0 to 4.3 kHz narrowband emission, and the $(n + 1/2)f_{ce}$ electron cyclotron harmonic waves. Because of the uncertainties involved, it is entirely possible that further investigation may lead to changes in some of the interpretations and possibly to new limits on the electron density profile. A complete understanding of the electron density in the inner region of the magnetosphere may not be possible until another mission to Neptune is carried out.

Acknowledgments. The authors would like to thank the Voyager team at the Jet Propulsion Laboratory for their valuable support in carrying out this investigation.

REFERENCES

Abdalla, M., and Kennel, C. F. 1978*a*. Nonconvective and convective electron cyclotron harmonic instabilities. *J. Geophys. Res.* 83:1531–1543.

Abdalla, M., and Kennel, C. F. 1978*b*. Multi-harmonic electron cyclotron instabilities. *Geophys. Res. Lett.* 5:711–714.

Aubier, M. G., Meyer-Vernet, N., and Pedersen, B. M. 1983. Shot noise from grain and particle impacts in Saturn's ring plane. *Geophys. Res. Lett.* 10:5–8.

Barbosa, D. D., and Kurth, W. S. 1990. Theory and observations of electrostatic ion waves in the cold Io torus. *J. Geophys. Res.* 95:6443–6450.

Barbosa, D. D., Kurth, W. S., Cairns, I. H., Gurnett, D. A., and Poynter, R. L. 1990. Electrostatic electron and ion cyclotron harmonic waves in Neptune's magnetosphere. *Geophys. Res. Lett.* 17:1657–1660.

Barkhausen, H. 1919. *Zwei mit Hilfe der neunen Verstarker entdeckte Ersheinungen. Phys. Z.* 20:401–403.

Belcher, J. W., Bridge, H. S., Bagenal, F., Coppi, B., Divers, O., Eviatar, A., Gordon, G. S., Jr., Lazarus, A. J., McNutt, R. L., Jr., Ogilvie, K. W., Richardson, J. D., Siscoe, G. L., Sittler, E. C., Jr., Steinberg, J. T., Sullivan, J. D., Szabo, A., Villanueva, L., Vasyliunas, V. M., and Zhang, M. 1989. Plasma observations near Neptune: Initial results from Voyager 2. *Science* 246:1478–1483.

Boardsen, S. A., Gallagher, D. L., Gurnett, D. A., Paterson, W. K., and Green, J. L. 1991. Funnel-shaped low frequency equatorial waves. *J. Geophys. Res.* 97:14967–14976.

Burns, J. A., Showalter, M. R., Cuzzi, J. N., and Pollack, J. B. 1980. Physical processes in Jupiter's ring: Clues to its origin by Jove! *Icarus* 44:339–360.

Burns, J. A., Showalter, M. R., and Morfill, G. E. 1984. The ethereal rings of Jupiter and Saturn. In *Planetary Rings*, eds. R. Greenberg and A. Brahic (Tucson: Univ. of Arizona Press), pp. 200–274.

Burns, J. A., Schaffer, L. E., Cuzzi, J. N., and Gurnett, D. A. 1986. Dust in the Uranian system: Its origin and fate. *Bull. Amer. Astron. Soc.* 18:770–771.

Cairns, I. H., Smith, C. W., Kurth, W. S., Gurnett, D. A., and Moses, S. L. 1991. Remote sensing of Neptune's bow shock: Evidence for large scale shock motions. *J. Geophys. Res.* 96:19153–19169.

Christiansen, P., Gough, P., Martelli, G., Bloch, J. J., Cornilleau, N., Etcheto, J., Gendrin, R., Jones, D., Béghin, C., and Décréau, P. 1978. GEOS 1: Identification of natural magnetospheric emissions. *Nature* 272:682–686.

Connerney, J. E. P., Acuña, M. H., and Ness, N. F. 1991. The magnetic field of Neptune. *J. Geophys. Res.* 96:19023–19042.

Eckersley, T. L. 1935. Musical atmospherics. *Nature* 135:104–105.

Filbert, P. C., and Kellogg, P. J. 1979. Electrostatic noise at the plasma frequency beyond the bow shock. *J. Geophys. Res.* 84:1369–1381.

Fredricks, R. W., Kennel, C. F., Scarf, F. L., Crook, G. M., and Green, I. M. 1968. Detection of electric-field turbulence in the Earth's bow shock. *Phys. Rev. Lett.* 21:1761–1764.

Grard, R., Nairn, C., Pedersen, A., Klimov, S., Savin, S., Skalsky, A., and Trotignon, J. G. 1991. Plasma and waves around Mars. *Planet Space Sci.* 29:89–98.

Gurnett, D. A. 1975. The Earth as a radio source: The nonthermal continuum. *J. Geophys. Res.* 80:2751–2763.

Gurnett, D. A., 1976. Plasma wave interactions with energetic ions near the magnetic equator. *J. Geophys. Res.* 81:2765–2770.

Gurnett, D. A., and Frank, L. A. 1976. Continuum radiation associated with low-energy electrons in the outer radiation zone. *J. Geophys. Res.* 81:3875–3885.

Gurnett, D. A., Shaw, R. R., Anderson, R. R., and Kurth, W. S. 1979. Whistlers observed by Voyager 1: Detection of lightning on Jupiter. *Geophys. Res. Lett.* 6:511–514.

Gurnett, D. A., Kurth, W. S., and Scarf, F. L. 1981*a*. Plasma waves near Saturn: Initial results from Voyager 1. *Science* 212:235–239.

Gurnett, D. A., Kurth, W. S., and Scarf, F. L. 1981*b*. Narrowband electromagnetic emissions from Saturn's magnetosphere. *Nature* 292:733–737.

Gurnett, D. A., Grün, E., Gallagher, D., Kurth, W. S., and Scarf, F. L. 1983*a*. Micron-sized particles detected near Saturn by the Voyager plasma wave instrument. *Icarus* 53:236–254.

Gurnett, D. A., Shawhan, S. D., and Shaw, R. R. 1983*b*. Auroral hiss, Z-mode radiation, and auroral kilometric radiation in the polar magnetosphere: DE 1 observations *J. Geophys. Res.* 88:329–340.

Gurnett, D. A., Kurth, W. S., Scarf, F. L., and Poynter, R. L. 1986. First plasma wave observations at Uranus. *Science* 233:106–109.

Gurnett, D. A., Kurth, W. S., Scarf, F. L., Burns, J. A., Cuzzi, J. N., and Grün, E. 1987. Micron-sized particle impacts detected near Uranus by the Voyager 2 plasma wave instrument. *J. Geophys. Res.* 92:14959–14968.

Gurnett, D. A., Kurth, W. S., Poynter, R. L., Granroth, L. J., Cairns, I. H., Macek, W. M., Moses, S. L., Coroniti, F. V., Kennel, C. F., and Barbosa, D. D. 1989. First plasma wave observations at Neptune. *Science* 246:1494–1498.

Gurnett, D. A., Kurth, W. S., Cairns, I. H., and Granroth, L. J. 1990. Whistlers in Neptune's magnetosphere: Evidence of atmospheric lightning. *J. Geophys. Res.* 95:20967–20975.

Gurnett, D. A., Kurth, W. S., Granroth, L. J., Allendorf, S. C., and Poynter, R. L. 1991. Micron-sized particles detected near Neptune by the Voyager 2 plasma wave instrument. *J. Geophys. Res.* 96:19177–19186.

Gurnett, D. A., Kurth, W. S., Granroth, L. J., Cairns, I. H., Macek, W. M., Poynter, R. L., Moses, S. L., Coroniti, F. V., Kennel, C. F., and Barbosa, D. D. 1992. Plasma wave observations at Neptune. *Adv. Space Res.* 12:(11)47–(11)54.

Helliwell, R. A. 1965. In *Whistlers and Related Ionospheric Phenomena* (Stanford, Calif.: Stanford Univ. Press).

Hubbard, R. F., and Birmingham, T. J. 1978. Electrostatic emissions between gyroharmonics in the outer magnetosphere. *J. Geophys. Res.* 83:4837–4850.

Jones, D. 1976. Source of terrestrial nonthermal radiation. *Nature* 260:686–689.

Jones, D. 1980. Latitudinal beaming of planetary radio emissions. *Nature* 288:225–229.

Kaiser, M. L., Connerney, J. E. P., and Desch, M. D. 1983. Atmospheric storm explanation of Saturnian electrostatic discharges. *Nature* 303:50–53.

Kaiser, M. L., Zarka, P., Desch, M. D., and Farrell, W. M. 1991. Restrictions on the characteristics of Neptunian lightning. *J. Geophys. Res.* 96:19043–19047.

Kennel, C. F., and Petschek, H. E. 1966. Limit on stably trapped particle fluxes. *J. Geophys. Res.* 71:1–28.

Kennel, C. F., Scarf, F. L., Fredricks, R. W., McGehee, J. H., and Coroniti, F.V. 1970. VLF electric field observations in the magnetosphere. *J. Geophys. Res.* 75:6136–6152.

Krimigis, S. M., Armstrong, T. P., Axford, W. I., Bostrom, C. O., Cheng, A. F., Gloeckler, G., Hamilton, D. C., Keath, E. P., Lanzerotti, L. J., Mauk, B. H., and Van Allen, J. A. 1989. Hot plasma and energetic particles in Neptune's

magnetosphere. *Science* 246:1483–1489.
Kurth, W. S., Barbosa, D. D., Gurnett, D. A., and Scarf, F. L. 1980. Electrostatic waves in the Jovian magnetosphere. *Geophys. Res. Lett.* 7: 57–60.
Kurth, W. S., Scarf, F. L., Gurnett, D. A., and Barbosa, D. D. 1983. A survey of electrostatic waves in Saturn's magnetosphere. *J. Geophys. Res.* 88:8959–8970.
Kurth, W. S., Strayer, B. D., Gurnett, D. A., and Scarf, F. L. 1985. A summary of whistlers observed by Voyager 1 at Jupiter. *Icarus* 61:497–507.
Kurth, W. S., Barbosa, D. D., Gurnett, D. A., and Scarf, F. L. 1987. Electrostatic waves in the magnetosphere of Uranus. *J. Geophys. Res.* 92:15225–15233.
Kurth, W. S., Barbosa, D. D., Gurnett, D. A., Poynter, R. L., and Cairns, I. H. 1990. Low-frequency radio emissions at Neptune. *Geophys. Res. Lett.* 17:1649–1652.
Menietti, J. D., Tsintikidis, D., Gurnett, D. A., and Curran, D. B. 1991. Modeling of Whistler ray paths in the magnetosphere of Neptune. *J. Geophys. Res.* 96:19117–19122.
Meyer-Vernet, N., Aubier, M. G., and Pedersen, B. M. 1986. Voyager 2 at Uranus: Grain impacts in the ring plane. *Geophys. Res. Lett.* 13:617–620.
Morfill, G. E., Grün, E., and Johnson, T. V. 1980*a*. Dust in Jupiter's magnetosphere: Physical processes. *Planet. Space Sci.* 28:1087–1100.
Morfill, G. E., Grün, E., and Johnson, T. V. 1980*b*. Dust in Jupiter's magnetosphere: Origin of the ring. *Planet. Space Sci.* 28:1101–1110.
Morgan, D. D., and Gurnett, D. A. 1991. The source location and beaming of terrestrial continuum radiation. *J. Geophys. Res.* 96:9595–9613.
Moses, S. L., and Coroniti, F. V. 1991. A mysterious plasma wave emission and the determination of plasma densities in Neptune's inner magnetosphere. *J. Geophys. Res.* 96:19013–19021.
Moses, S. L., Coroniti, F. V., Kennel, C. F., Kurth, W. S., and Gurnett, D. A. 1990. Comparison of plasma wave measurements in the bow shocks at Earth, Jupiter, Saturn, Uranus, and Neptune. *Geophys. Res. Lett.* 17:1653–1656.
Ness, N. F., Acuña, M. H., Burlaga, L. F., Connerney, J. E. P., Lepping, R. P., and Neubauer, F. M. 1989. Magnetic fields at Neptune. *Science* 246:1473–1478.
Northrop, T. G., and Hill, J. R. 1983. The adiabatic motion of charged dust grains in rotating magnetospheres. *J. Geophys. Res.* 88:1–11.
Olsen, R. C. 1981. Equatorially trapped plasma populations. *J. Geophys. Res.* 86:11235–11245.
Olsen, R. C., Shawhan, S. D., Gallagher, D. L., Green, J. L., Chappell, C. R., and Anderson, R. R. 1987. Plasma observations at the Earth's magnetic equator. *J. Geophys. Res.* 92:2385–2407.
Pedersen, B. M., Meyer-Vernet, N., Aubier, M. G., and Zarka, P. 1991. Dust distribution around Neptune: Grain impacts near the ring plane measured by the Voyager planetary radio astronomy experiment. *J. Geophys. Res.* 96:19187–19196.
Perraut, S., Roux, A., Roberts, P., Gendrin, R., Sauvand, J., Bosqued, J., Kremser, G., and Korth, A. 1982. A systematic study of ULF waves above FH+ from GEOS 1 and 2 measurements and their relationship with proton ring distributions. *J. Geophys. Res.* 87:6219–6236.
Pierce, E. T. 1977. Atmospherics and radio noise. In *Lightning*, ed. R. H. Golde (New York: Academic Press), pp. 351–383.
Richardson, J. D., Belcher, J. W., Zhang, M., and McNutt, R. L., Jr. 1991. Low-energy ions near Neptune. *J. Geophys. Res.* 96:18993–19012.
Rönnmark, K., Borg, H., Christiansen, P. S., Gough, M. P., and Jones, D. 1978. Banded electron cyclotron harmonic instability: A first comparison of theory and experiment. *Space Sci. Rev.* 22:401–417.
Russell, C. T., Holzer, R. E., and Smith, E. J. 1970. OGO 3 observations of ELF noise in the magnetosphere. 2. The nature of the equatorial noise. *J. Geophys. Res.*

75:755–768.
Sawyer, C., Warwick, J. W., and Romig, J. H. 1990. Smooth radio emission and a new emission at Neptune. *Geophys. Res. Lett.* 17:1645–1648.
Scarf, F. L., and Gurnett, D. A. 1977. A plasma wave investigation for the Voyager mission. *Space Sci. Rev.* 21:289–308.
Scarf, F. L., Fredricks, R. W., Frank, L. A., and Neugebauer, M. 1971. Nonthermal electrons and high-frequency waves in the upstream solar wind: 1. Observations. *J. Geophys. Res.* 76:5162–5171.
Scarf, F. L., Taylor, W. W. L., and Green, I. M. 1979*a*. Plasma waves near Venus: Initial observations. *Science* 203:748–750.
Scarf, F. L., Gurnett, D. A., and Kurth, W. S. 1979*b*. Jupiter plasma wave observations: An initial Voyager 1 overview. *Science* 204:991–995.
Scarf, F. L., Taylor, W. W. L., Russell, C. T., and Brace, L. H. 1980. Lightning on Venus: Orbiter detection of whistler signals. *J. Geophys. Res.* 85:8158–8166.
Scarf, F. L., Gurnett, D. A., Kurth, W. S., and Poynter, R. L. 1982. Voyager 2 plasma wave observations at Saturn. *Science* 215:587–594.
Schaffer, L., and Burns, J. A. 1987. The dynamics of weakly charged dust: Motion through Jupiter's gravitational and magnetic fields. *J. Geophys. Res.* 92:2264–2280.
Shaw, R. R., and Gurnett, D. A. 1975. Electrostatic noise bands associated with the electron gyrofrequency and plasma frequency in the outer magnetosphere. *J. Geophys. Res.* 80:4259–4271.
Smith, B. A., Soderblom, L. A., Banfield, D., Barnet, C., Basilevsky, A. T., Beebe, R. F., Bollinger, K., Boyce, J. M., Brahic, A., Briggs, G. A., Brown, R. H., Chyba, C., Collins, S. A., Colvin, T., Cook, A. F., II, Crisp, D., Croft, S. K., Cruikshank, D., Cuzzi, J. N., Danielson, G. E., Davies, M. E., DeJong, E., Dones, L., Godfrey, D., Goguen, J., Grenier, I., Haemmerle, V. R., Hammel, H., Hansen, C. J., Helfenstein, C. P., Howell, C., Hunt, G. E., Ingersoll, A. P., Johnson, T. V., Kargel, J., Kirk, R., Kuehn, D. I., Limaye, S., Masursky, H., McEwen, A., Morrison, D., Owen, T., Owen, W., Pollack, J. B., Porco, C. C., Rages, K., Rogers, P., Rudy, D., Sagan, C., Schwartz, J., Shoemaker, E. M., Showalter, M., Sicardy, B., Simonelli, D., Spencer, J., Sromovsky, L. A., Stoker, C., Strom, R. G., Suomi, V. E., Synott, S. P., Terrile, R. J., Thomas, P., Thompson, W. R., Verbiscer, A., and Veverka, J. 1989. Voyager 2 at Neptune: Imaging science results. *Science* 246:1422–1449.
Sonwalkar, V. S., Inan, U. S., and Bell, T. F. 1995. An interpretation of mysterious 3.0–4.6 kHz emission band observed on Voyager 2 near Neptune. *J. Geophys. Res.* 100:1795–1809.
Stix, T. H. 1962. *The Theory of Plasma Waves* (New York: McGraw-Hill)
Stone, E. C., and Miner, E. D. 1989. The Voyager 2 encounter with the Neptunian system. *Science* 246:1417–1421.
Storey, L. R. O. 1953. An investigation of whistling atmospherics. *Phil. Trans. Roy. Soc. London* 246A:113–114.
Taylor, H. A., and Cloutier, P. A. 1986. Venus: Dead or alive? *Science* 234:1087–1093.
Taylor, W. W. L., Scarf, F. L., Russell, C. T., and Brace, L. H. 1979. Evidence for lightning on Venus. *Nature* 282:614–616.
Tyler, G. L., Sweetnam, D. N., Anderson, J. D., Borutzki, S. E., Campbell, J. E., Eshleman, V. R., Gresh, D. L., Gurrola, E. M., Hinson, D. P., Kawashima, N., Kursinski, E. R., Levy, G. S., Lindal, G. F., Lyons, J. R., Marouf, E. A., Rosen, P. A., Simpson, R. A., and Wood, G. E. 1989. Voyager radio science observations of Neptune and Triton. *Science* 246:1466–1473.
Warwick, J. W., Pearce, J. B., Peltzer, R. G., and Riddle, A. C. 1977. Planetary radio astronomy experiment for the Voyager missions. *Space Sci. Rev.* 21:309–327.

Warwick, J. W., Evans, D. R., Romig, J. H., Alexander, J. K., Desch, M. D., Kaiser, M. L., Aubier, M., Leblanc, Y., Lecacheux, A., and Pedersen, B. M. 1982. Planetary radio astronomy observations from Voyager 2 near Saturn. *Science* 215:582–587.

Warwick, J. W., Evans, D. H., Romig, J. H., Sawyer, C. B., Desch, M. D., Kaiser, M. L., Alexander, J. K., Carr, T. D., Staelin, D. H., Gulkis, S., Poynter, R. L., Aubier, M., Boischot, A., Leblanc, Y., Lecacheux, A., Pedersen, B. M., and Zarka, P. 1986. Voyager 2 radio observations of Uranus. *Science* 233:102–106.

Warwick, J. W., Evans, D. R., Peltzer, G. R., Peltzer, R. G., Romig, J. H., Sawyer, C. B., Riddle, A. C., Schweitzer, A. E., Desch, M. D., Kaiser, M. L., Farrell, W. M., Carr, T. D., dePater, I., Staelin, D. H., Gulkis, S., Poynter, R. L., Boischot, A., Genova, F., Leblanc, Y., Lecacheux, A., Pedersen, B. M., and Zarka, P. 1989. Voyager planetary radio astronomy at Neptune. *Science* 246:1498–1501.

Zarka, P., and Pedersen, B. M. 1986. Radio detection of Uranian lightning by Voyager 2. *Nature* 323:605–608.